Accepted Manuscript

Effects of sedimentation on rift segment and transfer zone evolution in orthogonal and oblique extension settings: Insights from analogue models analysed with 4D X-ray computed tomography and digital volume correlation techniques

Frank Zwaan, Guido Schreurs, Jürgen Adam

PII: S0921-8181(17)30236-9
DOI: doi:10.1016/j.gloplacha.2017.11.002
Reference: GLOBAL 2668

To appear in: *Global and Planetary Change*

Received date: 15 May 2017
Revised date: 30 October 2017
Accepted date: 3 November 2017

Please cite this article as: Frank Zwaan, Guido Schreurs, Jürgen Adam , Effects of sedimentation on rift segment and transfer zone evolution in orthogonal and oblique extension settings: Insights from analogue models analysed with 4D X-ray computed tomography and digital volume correlation techniques. The address for the corresponding author was captured as affiliation for all authors. Please check if appropriate. Global(2017), doi:10.1016/j.gloplacha.2017.11.002

This is a PDF file of an unedited manuscript that has been accepted for publication. As a service to our customers we are providing this early version of the manuscript. The manuscript will undergo copyediting, typesetting, and review of the resulting proof before it is published in its final form. Please note that during the production process errors may be discovered which could affect the content, and all legal disclaimers that apply to the journal pertain.

ACCEPTED MANUSCRIPT

Effects of sedimentation on rift segment and transfer zone evolution in orthogonal and oblique extension settings: insights from analogue models analysed with 4D X-ray computed tomography and digital volume correlation techniques

Frank Zwaan*[1], Guido Schreurs[1], Jürgen Adam[2]

1) Institute of Geological Sciences, University of Bern, Baltzerstrasse 1+3, CH-3012 Bern, Switzerland
2) Department of Earth Sciences, Royal Holloway, University of London, Egham, Surrey, TW20 0EX, United Kingdom
*E-mail: frank.zwaan@geo.unibe.ch

Keywords: analogue modelling, extensional tectonics, sedimentation, transfer zone, X-ray computed tomography (XRCT), digital volume correlation (DVC) analysis

Abstract

During the early evolution of rift systems, individual rift segments often develop along pre-existing crustal weaknesses that are frequently non-continuous and laterally offset. As extension progresses, these initial rift segments establish linkage in order to develop a continuous rift system that might eventually lead to continental break-up. Previous analogue and numerical modelling efforts have demonstrated that rift interaction structures are influenced by structural inheritances, detachment layers, magma bodies, rate and direction of extension, as well as distance between rift segments on rift interaction structures. Yet to date, the effects of syn-tectonic sediments have been largely ignored or only modelled in 2D. In this study we therefore assess the influence of sedimentation on rift segment and rift transfer zone evolution in orthogonal and oblique extension settings, by means of 3D brittle-ductile analogue models, analysed with 4D X-ray computed tomography (XRCT or CT) methods and 3D digital volume correlation (DVC) techniques.

Our models show that syn-rift sedimentation does not significantly influence the large-scale evolution of rift and transfer zone structures. Nevertheless, syn-rift sedimentation can strongly affect rift-internal structures: sedimentary loading reinforces the rift wedge, decreasing rift wedge faulting and increases subsidence within the rift basin. These effects are strongest in areas where most accommodation space is available, that is, along the main rift segments. In contrast, rift segments that undergo high degrees of oblique extension develop less accommodation space and are therefore less influenced by sedimentary loading. Rift interaction structures are least affected by sediment influx, as they experience

ACCEPTED MANUSCRIPT

relatively low amounts of subsidence and little accommodation space is available. Our conclusions are valid for the early stages of rift development, when a high sediment influx could delay continental break-up, as other processes are likely to become dominant during later stages of continental extension. Finally state-of-the-art DVC analysis of CT data proves to be a powerful tool to extract and fully quantify 3D internal model deformation in great detail and could be useful for comparing and calibrating analogue and numerical models.

ACCEPTED MANUSCRIPT

ACCEPTED MANUSCRIPT

1. Introduction

Early rifting of the continental lithosphere involves the formation of rift segments, usually along the trace of pre-existing tectonic fabrics (e.g. Morley et al., 1990). As the system evolves, these rift segments, which are often non-continuous and offset, must grow laterally, interact and connect in order to create a continuous rift basin on the way to continental break-up, for instance in the East African Rift System (Fig. 1a, b). Associated rift interaction structures are called either transfer zones, where hard linkage occurs and continuous fault zones connect rift segments, or accommodation zones involving soft linkage, where rift boundary faults do not yet connect (Rosendahl, 1987; Larsen, 1988; Childs et al., 1995; Faulds and Varga, 1998, Fig. 1c, d). The evolution of rift interaction structures during early rift development is of importance because of its control on melt migration, the localization of volcanic activity and a better understanding may improve seismic risk assessment (Lambiase and Bosworth, 1995; Faulds and Varga, 1998 and references therein; Acocella et al., 1999a,b, Corti et al., 2004). Developing rift interaction zones are also known to influence hydrocarbon systems, by controlling the drainage and sedimentation patterns leading to source rock and reservoir rock deposition (Roberts et al., 1990; Faulds and Varga, 1998). Furthermore, the complex structuration affects the migration of hydrocarbons (Nelson et al., 1992; Acocella et al., 1999a,b; Corti et al., 2004), and facilitates formation of hydrocarbon traps as observed in the North Sea Viking Graben and the East African Rift System (Morley et al., 1990; Fossen et al., 2010).

Previous analogue and numerical modelling studies have demonstrated the influence of inherited structures, detachment layers and magma bodies, as well as distance between rift segments on rift interaction structures (e.g. Basile and Brun, 1999; Le Calvez and Vendeville, 2002; Paul and Mitra, 2013; Zwaan et al., 2016). Other important factors are the rate and direction of extension. High strain rates strengthen the ductile parts of the lithosphere (Brun, 1999; Buiter et al., 2008). Associated high brittle-ductile coupling effects generate distributed or wide rifting, hindering rift linkage whereas, low strain rates/viscosities tend to localize extension in narrow rift zones, favouring transfer zone formation (Allken et al., 2011, 2012; Zwaan et al., 2016). Recent studies demonstrate that oblique extension has an important influence on rift linkage as it either causes rift segments to propagate toward each other or to grow away from each other, depending on the initial rift segment configuration (Zwaan and Schreurs, 2017). Within the context of oblique extension facilitating continental break-up as the plastic yield limit is reached earlier than under orthogonal extension conditions (Brune et al., 2012), oblique extension may also assist break-up on a crustal scale by promoting of rift segment linkage.

ACCEPTED MANUSCRIPT

Also surface processes are known to affect tectonic systems, erosion for instance can significally increase orogenic topography (Simpson, 2006) and localize crustal deformation (Stolar et al., 2007), while syn-collisional sedimentation may cause subduction plate retreat and diffused crustal deformation (Gray and Pysklywec, 2012). Similarly, erosion affects extensional systems, for instance prolonging fault activity and increasing rift subsidence (Burov and Poliakov, 2001; Olive et al., 2014). Syn-rift sedimentation can have an important effect on extensional tectonic settings as well, suppressing salt diapirism (Thomas, 1994; Brun and Fort, 2008), causing rifting to shift to a narrow rifting mode (Bialas and Buck, 2009) or even delaying continental break-up (Martín-Barajas et al., 2013).

However, previous attempts to model the coupling between surface processes and rift tectonics have predominantly been based on 2D simulations. In this study we therefore assess the influence of sedimentation on rift and rift interaction structures in orthogonal and oblique extension settings in 3D, by means of three series of crustal scale brittle-ductile analogue models that are analysed with state-of-the-art 4D X-ray Computer Tomography (XRCT or CT) methods and 3D Digital Volume Correlation (DVC) techniques.

2. Materials and methods

2.1 Material properties

We use both brittle and viscous materials to simulate the brittle and ductile parts of the continental crust, respectively. A 4 cm thick layer of fine quartz sand (ø = 60-250 µm), sieved from ca. 30 cm height into the model to ensure a constant density of ca. 1560 kg/m^3, acts as a 20 km thick brittle upper crust. The sand is also flattened with a scraper at every cm during model construction, which creates slight density differences. This “layering” subsequently appears on CT images but is not considered to have a significant influence on subsequent material behaviour (Fig. 2h). Sedimentary infill is modelled with alternations of fine corundum and quartz sand as the density differences between both sand types is visible on CT images (ρ = 1890 kg/m^3 and ø = 88-175 µm for corundum sand, Panien et al., 2006; Klinkmüller, 2011).

We apply a 4 cm thick viscous layer to simulate a 20 km thick lower crust. The viscous material is a mixture of the same corundum sand mentioned above with SGM-36 Polydimethylsiloxane (PDMS) silicone (weight ratio PDMS : corundum sand = 0.965 : 1.00). Its behaviour is near-Newtonian (η = ca. $1.5 \cdot 10^5$ Pa·s; n = 1.05) and the viscous mixture has a similar density as the overlying quartz sand (ca. 1600 kg/m^3). This results in a more natural

ACCEPTED MANUSCRIPT

density profile than pure PDMS would allow (ρ = ca. 960 kg/m^3) and it prevents undesirably strong buoyancy effects.

Small quantities of Zirshot ceramic microbeads (ρ = ca. 2300 kg/m^3 and ø = 150-210 µm, Carlo AG, 2017) are mixed with the quartz and corundum sands in a 1:50 weight ratio to generate a volumetric pattern on CT scans, allowing DVC analysis (Adam et al., 2013, see section 2.4). Note that the 1:50 weight ratio corundum/Zirshot mixture is itself mixed with the PDMS, so that the actual Zirshot weight ratio is ca. 1:100 in the viscous layer. The Zirshot spheres are not considered to have a significant effect on the behaviour of the main model materials (Lohrmann et al., 2003, Panien et al., 2006, Klinkmüller, 2011). Further material properties are summarized in Table 1.

2.2. Experimental set-up

The experimental apparatus consists of a 36 cm wide base of foam and Plexiglass bars between two longitudinal sidewalls, which is compressed to a 30.5 cm width before model materials are applied (Fig. 2a, c, g, l). As precise computer-controlled motors drive the sidewalls apart during an experiment, the foam expands, which causes distributed extension that is transferred to the overlying model materials with minimal boundary effects (Fig. 2g). One base plate can move laterally, which in combination with the outward motion of the longitudinal sidewalls, allows the application of any required degree of oblique extension (Fig. 1b, Fig. 2a, d-f, k, m). At both ends of the model, pivoting plastic bars control the model base when oblique extension is applied by forcing the Plexiglass bars with the foam stacked in between sideways, into a parallelogram shape (Fig. 2a, d-f). Rubber sidewalls contain the model ends and accommodate distributed deformation, reducing boundary effects (Fig. 2a). Every component of the machine around the model consists of X-ray transparent materials to allow for CT-scanning and various models are analysed with CT-techniques to reveal their 3D internal evolution (Fig. 2b, g, l).

Thin rods (1 cm thick, semi-cylindrical) of the PDMS/corundum sand mixture are applied on top of the basal viscous layer (Fig. 2a). These “seeds” act as linear weak zones, representing discrete crustal weaknesses; the strong sand layers above the seeds are locally thinner and thus weaker, causing deformation to localize (Fig. 2c, g, h-i, l, m). We use a disconnected “staircase offset” seed geometry for model series 1 (φ = 90°, no seed over- or underlap, Fig. 2h and m). Series 2 and 3 both involve a secondary rift-connecting seed, representing a secondary structural grain as for instance observed in the Rhine-Bresse transfer zone (Ustaszewski et al., 2005) and the East Africa Rift System (Acocella et al.,

ACCEPTED MANUSCRIPT

1999a and references therein, Figs. 1a, 2i, j). The seed offset is 2 H in all set-ups (Fig. 2h-j, m), H being equivalent to the brittle layer thickness, in order to avoid rift proximity effects (Zwaan et al., 2016). A 4x4 cm grid allows the tracking of surface deformation (Fig. 2a).

Extension obliquity is defined by the angle α between the normal to the seed orientation and the extension direction (Fig. 2k). When α is zero, extension is orthogonal, a positive angle α indicates dextral oblique extension and a negative angle α implies sinistral oblique extension. We apply orthogonal extension and various degrees of dextral oblique extension for series 1 (α = 0˚, 30˚ or 60˚). Series 2 involves slight dextral oblique extension (α = 15˚), whereas we use sinistral oblique extension (α = -30˚) for series 3 (Table 2).

Every model run takes 4 hours and with an extension rate of 7.5 mm/h results in a total of 30 mm extension in the specified direction (Fig. 2i). Most models were run twice: once with and once without syn-rift sedimentation for comparison. Sedimentation is implemented by filling the rift basins with alternating layers of quartz and corundum sand. This is done by hand at fixed time steps, (t = 1h, 2h and 3h, Fig. 2l, m), with the use of a small funnel, after which a slight amount (ca. 0.5 mm) of quartz sand was sieved on the surface to cover the brown corundum sand for better top view quality and subsequently a new grid was made. Sedimentation in our models is thus not a continuous process. This is in rough accordance with the observation that sedimentation in natural rift settings generally occurs in cyclothems, that is pulses associated with recurring periods of fault reactivation (Martins-Neto and Catuneanu, 2012). Although the application of sediment is instantaneous and therefore not completely realistic, the periodicity (and thus magnitude) of cyclotems in rifts is 2-15 Ma (Blair and Bilodeau, 1988), fitting reasonably well with the scaled timeframe of our experiments (section 2.3), providing us with a useful first-order comparison between the system with and without sedimentation.

We applied 20 min time steps (2.5 mm of extension) for CT-scanning, to acquire a detailed record of the 3D model evolution. During these scans, the model was halted (ca. 5 min) to acquire multiple CT datasets per time step, improving data quality for subsequent DVC analysis. The model was also stopped during sediment application, allowing a small timeframe (ca. 10 min) in which the model deforms slightly, as revealed by DVC results between the pre- and post-sediment scans of the same time step. This deformation is however insignificant with respect to the displacements induced by the experimental apparatus when the model is running. We completed 14 experiments in total, of which further details are shown in table 2.

ACCEPTED MANUSCRIPT

2.3. Model scaling

In order to correctly represent crustal deformation, our models need to be properly scaled. Stress ratios (σ*, convention: $\sigma^* = \sigma_{model}/\sigma_{nature}$) can be calculated with the following equation (Hubbert, 1937; Ramberg, 1981): $\sigma^* = \rho^* \cdot h^* \cdot g^*$ (eq. 1), where ρ*, h* and g* represent the density, length and gravity ratios respectively. The strain rate ratio $\dot{\varepsilon}^*$ can be calculated with the stress ratio σ* and the viscosity ratio η* (Weijermars and Schmeling, 1986): $\dot{\varepsilon}^* = \sigma^*/\eta^*$ (eq. 2), which allows us to derive the velocity ratio v* and time ratios t* using the following equations: $\dot{\varepsilon}^* = v^*/h^* = 1/t^*$ (eq. 3 and eq. 4). Assuming an intermediate natural lower crustal viscosity of 10^{21} Pa·s (e.g. Buck 1991), an hour in our model represents 0.84 Ma and our extension velocity translates to ca. 4.5 mm/y, which is very similar to extension velocities observed in nature (a few mm/y, e.g. Saria et al., 2014, Fig. 1b). The values we use for our scaling calculations are listed in Table 3.

To ensure dynamic similarity between brittle materials in our models and nature, we apply the ratio R_s as a function of gravitational stress and cohesive strength or cohesion C (Ramberg, 1981; Mulugeta, 1998): $R_s = gravitational\ stress/cohesive\ strength = \rho \cdot g \cdot h/C$ (eq. 5). Furthermore, we use the Ramberg number R_m for viscous materials (Weijermars and Schmeling, 1986): $R_m = gravitational\ stress/viscous\ strength = \rho \cdot g \cdot h^2/(\eta \cdot v)$ (eq. 6). The model Ramberg number of 80 is close to the natural value of 120 and the R_s values are quite similar in our models and nature as well: 25.5 and 9.2, respectively.

ACCEPTED MANUSCRIPT

2.4. Digital Volume Correlation (DVC)

2.4.1. General methodology

Besides revealing the internal structures of our models in great detail at various time steps, the use of CT techniques also allows the application of digital volume correlation (DVC) to quantify 3D internal model deformation. DVC analysis, which is based on cross correlation of intensity patterns in time-series voxel data, has a significant advantage over preceding techniques (e.g. 3D PIV, Boutelier et al., 2012; Strak and Schellart, 2014) as it enables a full quantification of 3D displacement fields and the derived 3D strains and strain rates within otherwise opaque model materials. Furthermore, DVC does not trace individual particles, but particle patterns, which makes it an ideal technique to analyse larger 4D datasets with strong deformation gradients (Adam et al., 2005; Adam et al., 2013).

We use the DVC module of the commercial DaVis image correlation software package (version 8.4, © LaVision). The DVC algorithm calculates model displacement fields by cross correlating intensity patterns in small voxel sub-volumes of the time-series experiment volume. For small sub-volumes, local displacement vectors are determined by identifying similar intensity patterns of individual voxel sub-volumes in subsequent time steps of the experiment volume (Fig. 3a, b). The digital cross correlation of the 3D intensity patterns is executed by Fast Fourier Transform (FFT) algorithm, which provides the spatial average of the local displacement vectors over the size of the voxel sub-volume (Fig. 3c). Subsequently, the incremental displacement field is constructed by assembling the 3D vectors of all sub-volumes in the voxel space.

Although DVC analysis does not require the identification of individual particles in voxel sub-volumes, small-scale intensity variations caused by identifiable particle clusters are essential for the calculation of a high-resolution displacement field. In order to improve the texture on the CT-data, the models were scanned multiple (five) times for every 20 min time step and the intensity values of the voxel data are subsequently stacked. This reduces the noise caused by the high X-ray reflectivity of the Zirshot ceramic beads, significantly improving the clarity of the intensity patterns and consequently the quality of the DVC results. Furthermore, pre-processing image filters serve to enhance the image texture and to further eliminate background noise.

With the incremental displacement field, displacement components (v_x, v_y, v_z) and the derived strain tensor $E_{ij} = \partial V_i / \partial_j$ (with $i \in \{x, y, z\}$ and $j \in \{x, y, z\}$) can be calculated.

ACCEPTED MANUSCRIPT

Subsequently, the strain tensor E_{ij} allows us to determine incremental shear strain (ε_{xy}, ε_{xz}, ε_{yz}) and the 3D Shear (3Ds = $|\vec{\varepsilon}_x - \vec{\varepsilon}_z|$). The incremental displacement and strain data describe material transport and deformation between successive scans, as well as their spatial and temporal variation in the experiments. Moreover, the total displacement field and finite strain in the experiment volume can be determined by Lagrangian summation of the incremental displacement data (e.g. geological strain, Fig. 3e and 3f).

2.4.2. Vector resolution

The spatial resolution or density of the vector field depends on the voxel size, sub-volume size and overlap of the sub-volumes. The voxel size (voxel = volume pixel) depends on the XRCT scanner resolution (voxel size = 0.6 mm in this study). The sub-volume and overlap of the sub-volumes are DVC analysis parameters depending on the combination of scanner resolution and the quality of intensity patterns in the granular material.

The sub-volumes must remain large enough to include characteristic elements of the image texture for a reliable correlation between successive time-series images of the experiment volume. A robust identification of distinct intensity patterns in the experiment volume was achieved with sub-volumes of 32*32*32 voxels (sub-volume size = 32 voxels) and consequently each 3D displacement vector represents the spatial average of a discrete experiment volume with the size of 19.2 x 19.2 x 19.2 mm or 7.1 cm3.

The high spatial vector resolution was achieved by calculating vectors for overlapping sub-volumes. In our experiments with a sub-volume size of 32 voxels and a 75% overlap the vector resolution is 8 voxels. Consequently, the resulting vector resolution is 4.8 mm or approximately 32 times D50 for the given voxel size (0.6 mm) of the scanner and mean grain size of the silica sand (grain size = 60-250 micron with D50 ~ 0.15 mm). The small sub-volumes and high vector resolution enable the observation of inhomogeneous translation and deformation in the experiment volumes.

2.4.3. Vector accuracy

Modern DVC cross-correlation algorithms achieve vector accuracies significantly smaller than 0.1 voxel with ranges from 0.05 to 0.1 voxel depending on the sub-volume size, image quality and image texture (Liu & Morgan, 2007; Pannier et al., 2010). The use of FFT algorithm in combination with the multi-pass approach in the local correlation used in the

ACCEPTED MANUSCRIPT

StrainMaster DVC system (DaVis 8.4, © LaVision) allowed displacement uncertainties ranging between 0.006 voxel and 0.02 voxel (Madi et al., 2013). However, these error margins not only depend on the accuracy of the mathematical correlation procedures but also on the quality of the volume data. Assuming the higher error margin of 0.1 voxel, the vector accuracy for the DVC analysis of the experiments is ±0.06 mm (±0.4 D50).

3. Model results

3.1. Series 1 models

3.1.1 Top view analysis

A surface overview of models from series 1 is presented in Fig. 4. Deformation initially localizes above the seeds where rift segments start to form. Our models demonstrate the dominant influence of the extension direction on the propagating rift segments. When extension is orthogonal, the rifts propagate slightly towards each other (Fig. 3a). An extension obliquity of 30˚ causes the rifts to propagate towards each other in a more acute angle (ca. 40˚ oblique with respect to the rift trend, Fig. 4b, e). This effect is even more pronounced in the case of. 60˚ extension obliquity with respect to the rift trend (Fig. 4c, f). The curved character of the rift propagation creates a horst or “rift pass” structure (Nelson et al., 1992) between the propagating rift branches, although its size diminishes with increasing extension obliquity (Fig. 4a-c). This rift pass represents a zone of elevated viscous material as revealed by the topography of the viscous layer after sand removal (Fig. 4d-f), and undergoes some sinistral rotation around a vertical axis (Fig. 4a). Final rift width decreases with increasing extension obliquity from ca. 4.5 cm in orthogonal extension models to ca. 2.4 cm in the 60˚ oblique extension case, Fig. 8a). Simultaneously, a higher degree of oblique extension promotes the formation of oblique rift-internal structures (Fig. 4c).

The above-mentioned general features also occur in models with syn-rift sedimentation (Fig. 4g-j). However, the regular filling of the rift basins results in significantly less pronounced rift topography. In models without sedimentation the seed below the rift segments rises towards the model surface as is visible after sand removal (Fig. 4d-e). In models with sedimentation the same “diapirism” occurs but an additional trough structure develops within the seed, which continues partially into the propagating rift branch (Fig. 4i, j).

3.1.2. CT-analysis

The use of X-Ray CT techniques allows a more detailed analysis of our models (Figs. 5-7). Almost immediately after experiment initiation faults localize above the seed (Figs. 6d, j, 7d,

ACCEPTED MANUSCRIPT

j) and subsequently rift basins develop after some 40 to 60 min, or 5 to 7.5 mm of extension (Figs. 5b, f, j, n, 6e, k, q, w). These grabens remain separated in the orthogonal extension cases, but the oblique extension models establish rift linkage early on (after some 120 min or 15 mm extension, Fig. 5k, o). As the model run proceeds and the rift branches propagate, the developing rift pass areas undergo relative uplift. The latter is highlighted in Fig. 5c, d, g, h, k, l, o, p, since the most elevated parts of the model form a lesser barrier for X-rays and are subsequently brighter (see also Figs. 6a, b, sections 3-5 and 10-12 and Fig. 7a, b, sections 3-5 and 10-13). The same bright colours suggest rift shoulder uplift along the main rift boundary faults (Fig. 5).

2D CT-sections provide a detailed insight into the internal structuration and evolution (Figs. 6 and 7). By combining these 2D sections, the internal structural variation can be shown in 3D (Figs. 6a, b and 7a, b). Under orthogonal extension and independently from the presence of syn-rift sediments, the sections indicate that the rifts are most complex above the initial seeds (Fig. 6a, b). The propagating parts of the rift segments have similar characteristics, although they are less developed than the sections above the initial seeds. In both models, the rift structure is bounded by two major boundary faults that have accumulated less slip towards the propagating rift tip (Figs. 6a, b). However, the features within the rifts are strongly influenced by the presence of sedimentation, which can be best observed in the main rift segments, where most deformation is accommodated (Fig. 6o-t and u-z).

The topography of the rift valley floors is quite distinct. Without syn-rift sediments (Model B), the rift valley floors exhibit a deep bowl-like shape (Fig. 6a, h and n), whereas the topography is rather flat when sedimentation is applied (Model C, Fig. 6b, t and z) Furthermore, the rift wedge is much more deformed and faulted in Model B, as shown by the dark grey colours (Fig. 6a, h and n) and its rift boundary faults angle decrease with time (from initially ca. 70˚ to ca. 60˚ towards the end of the model run, see Fig. 6e-h, k-n and Fig. 8e). In contrast, Model C develops localized deformation along fewer large faults within the rift wedge (Fig. 6b, t and z) and its rift boundary fault angle remains the same throughout the model run (ca. 70˚, Fig. 8f). An additional feature is the geometry of the seed underneath the rift structure. As already seen on top view images (Fig. 4d-f, i and j), the seeds rise under the rifts in all models, but the rift wedge sinks deeper into the seed when sediments are applied, causing the viscous layer to rise less and form a deep V-shaped depression on the seed crest (Fig 6h', n', t' and z'). Syn-rift sedimentation thus results in stronger subsidence: the earliest syn-rift sediments in Model C subside deeper than the rift valley floor does in Model B (compare h' and n' with t' and z' in Fig. 6, Fig 8b).

ACCEPTED MANUSCRIPT

Under 30˚ oblique extension conditions, the rifts connect, creating a complex transfer zone with a fully-developed rift pass in between (Fig. 7a and b). However, the overall picture is rather similar to the orthogonal extension situation. Again, the main rift segments along the seeds contain the best-developed structures, which become less complex towards the propagated tips, where they may merge with the adjacent rift segment (seen in Figs. 5i-l, m-p and 7b, section 14). The rift segments show the same response to syn-rift sedimentation as seen in the previous orthogonal extension models. We obtain a flatter rift valley topography, the rift wedge exhibits a strongly localized deformation along major faults instead of a shattered appearance, and significantly more subsidence occurs (compare Fig. 7 h, h', n, n' with Fig. 7t, t', z, z'). In comparison to the orthogonal extension case, however, the rift boundary faults are steeper, the rift basins are narrower and less subsidence occurs (measurements summarized in Fig. 8).

3.1.3. Digital Velocity Correlation (DVC) analysis of Model B

The use of DVC techniques allows us to fully quantify the internal model displacement field and related deformation processes. We present the first DVC results in a range of colour charts that display the various displacement (Fig. 9) and strain components (Fig. 10) for Model B, as it is the least complex model (orthogonal extension, no sedimentation). The finite displacement and strain results are visualised in three sections (xy – normal to rift zones) that represent sections 2, 4 and 6 of Model B (see Fig. 5d and 6a for their locations), quantifying the sum displacement and strain of the model at the end of the experiment.

Figure 9a-c shows the finite 3D displacement field (v_l, the colour chart shows finite 3D displacement, white arrows represent the 3D vectors projected in xy-plane). The three displacement components in x, y and z-directions illustrate the horizontal displacement parallel to the sections (v_x: Fig. 9d-f), the vertical displacement (v_y: Fig. 9g-i) and the horizontal out-of-plane displacement perpendicular to the xy-plane (v_z: Fig. 9j-l). The 3D displacement chart (Fig. 9a-c) illustrates the contrasting deformation styles in the brittle sand layer and viscous layer as well as the localised deformation in the rift basins, whereas the central horst structure between the rift segments is characterised by small displacements, reflecting its relative stable position. The high displacement zone in the viscous layer near the left model boundary is probably due to boundary effects (limited normal faulting, Fig. 7a, d).

ACCEPTED MANUSCRIPT

The horizontal displacement chart (v_x) illustrates model extension normal to the rift segments with the left-hand and right-hand halves of the model roughly moving in opposite directions (Fig. 9d-f). Horizontal displacement is strongest in the silicone layers close to the sidewalls and different displacement patterns are noticeable in the brittle and ductile layers. In the sand layer the pronounced displacement continuity is located in the most active rift segment whereas material moves differently in the silicone layer beneath the central horst structure (Fig. 9d, f). The brittle part of the horst behaves as a solid block, as indicated by the continuous colour, and moves away from the dominant rift, yet slower than the adjacent brittle units (Fig. 9d-f). Below the horst, parts of the viscous layer flow towards the most dominant rift (shown by thick white arrows in Fig. 9d-f).

The vertical displacement chart (v_y, Fig. 9g-i) displays areas of subsidence and uplift in the xy-plane. It is dominated by general subsidence throughout the model because of the overall stretching of the viscous layer. Yet subsidence is strongest in the rift basins and toward the sides of the model, whereas the central horst remains relatively stable. In addition, below the large rift structures, the viscous layer shows strong upward flow due to thinning and unloading of the overlying sand layers in the rift segments (Fig. 9g and i). This phenomenon is also present, although less pronounced, in the central section of the model, where the two rifts in the overlap zone are comparable in size (Fig. 9h).

Horizontal displacement perpendicular to the xy-plane (v_z) and parallel to the rift axis is less pronounced than observed for the x and y directions (max. 4 mm instead of up to 10 mm) and is strongest in the viscous layer of the left-hand side of the model (Fig. 9j-k). Here, material moves out of section, towards the observer. Out-of-section displacement is most prominent in the left-central section of the model, away from the boundary walls (Fig 9k). In the viscous layer beneath the central horst a counter flow occurs (Fig 9k, on the left side material moves towards the observer and on the right side it moves away). These dominant flow directions are also observable in the respective overlying rift segments, between which a displacement gradient indicates a small strike-slip component (oblique-slip rift faults: dextral in left rift; sinistral in right rift as seen in Fig. 10k) caused by minor rotation of the central horst block about a vertical axis (Fig. 4a).

From the 3D displacement field, the 3D strain field and related strain components can be derived (Fig. 10a-c). Similar to the displacement components, the strain data are shown in xy-sections colour charts. In addition to the overall 3D shear strain (Fig. 10a-c), we show the longitudinal strain (e_{xx}) indicating extension and contraction in x-direction normal to the rift segments (Fig. 10d-f), shear strain (e_{xy}) indicating sinistral and dextral shear in the xy-plane

ACCEPTED MANUSCRIPT

(Fig. 10g-i), and longitudinal strain (e_{zz}) visualising extension and contraction along the z-axis normal to the xy-section and parallel to the rift segments (Fig. 10d-f). The total 3D shear strain plots show a strong contrast between the lower viscous layer and the upper brittle layer; the strain is distributed along the top and basal interface of the viscous layer, whereas strain in the brittle sand layer is strongly localized along the major rift fault zones with shear strains up to 30% (Fig. 10a-c).

An important contributor to the 3D strain field is the longitudinal strain along the x-axis (e_{xx}, Fig. 10d-f). Extension strain values up to 25% characterise the main rift segments, while the rising viscous material below the rifts indicate convergent flow and contraction with strain values around -10%. Along the sidewalls, slight boundary effects are visible. In the other parts of the model, the viscous layer shows a generally distributed extension with maximum finite strain values of approximately 10% in the centre of the viscous layer indicating channel flow.

Planar shear strain (e_{xy}) charts indicate areas of sinistral and dextral shear in the xy plane (warm colours and cold colours, respectively; Fig. 10g-i). The conjugate rift boundary faults show contrasting shear sense with right-dipping faults exhibiting dextral shear (blue) and left-dipping faults showing sinistral shear (red) which is in agreement with the normal fault conditions. This configuration is not restricted to the brittle parts of the model as the faults extend into differential flow zones in the viscous layer with conjugate flow regimes. The best example is illustrated in Fig. 10i, in which two additional dextral and sinistral shear flow zones develop, accommodating the rise of viscous material below the rift as seen in Fig. 9i. The shear pattern observed near the sidewalls is probably due to boundary effects as seen on displacement field charts (Fig 9d-f).

In contrast to the e_{xx} and e_{xy} results, the longitudinal strain in z-direction (e_{zz}) is less structured (Fig. 10j-l). The longitudinal strain (e_{zz}) is very small in comparison to the perpendicular longitudinal horizontal strains in the extension direction (maximum e_{zz} ~ 1% and maximum e_{xx} ~ 25%, respectively) We generally observe strain localization in the rift structures within the brittle layer and more distributed strain in the viscous part of the model.

3.1.4. Digital Volume Correlation (DVC) analysis of Model C

Similar to Model B, DVC analysis was applied to Model C (orthogonal extension, with sedimentation) in order to allow a quantitative comparison between models with and without sedimentation (Fig. 11). The displacement fields are rather comparable to those of Model B,

ACCEPTED MANUSCRIPT

with displacement concentrated towards the sides of the model, while the horst block or rift pass in the middle of the model remains relatively stable (11a-f). Model C also shows the same type of boundary effects (strong displacement near the model edge). Displacement magnitudes are however slightly higher than those observed in Model B (Fig. 9a-f) as a consequence of the additional loading by syn-rift sediments, causing both sides of the model to slide away faster from the relatively stable central horst block.

Vertical displacement in Model C (Fig. 11g-h) has a similar character as seen in Model B (Fig. 11g-h). Overall subsidence occurs throughout the model, with localized uplift and subsidence at the developing rift basins. However, uplift of viscous material below the rifts is less intense under the main rift segments in Model C than in Model B (Fig. 9g, i and Fig. 11g, i) due to the synkinematic sediment loading. Yet, the rise of material below the rifts at the central horst block appears to be slightly stronger than observed in Model B (Fig. 9h and Fig. 11h). Another difference is visible in the areas adjacent to the main rift structures, where the darker colours and steeper vectors in Model C (Fig. 11g-h) indicate stronger subsidence than for the same areas in Model B without sedimentation (Fig. 9g-h).

Comparing the more detailed differences in total displacements and total strains within the rift wedges is not feasible at this stage, because the Lagrangian summation of the incremental displacement data is only possible for the pre-kinematic material present at the start of the experiment and cannot be applied to newly applied material. We must therefore refrain from discussing these parts of the model in detail, although subsidence is obvious (Fig 11g-i). Furthermore, material is moving out of plane, most importantly on the left-hand side of the mode, an observation previously also made in Model C (Fig. 9j-l and Fig. 11j-l). However, dynamics of faulting and the effect of synkinematic sedimentation could be analysed using the incremental displacement data, but the current DVC resolution does not allow a more detailed interpretation.

Overall, the results of the DVC analysis of Model C are rather comparable to those of Model B. The main differences lie in the higher displacement values that occur when syn-rift sedimentation is applied. As the results of the strain analysis for Model C are almost identical to those of Model B, they are not further discussed here. For the Model C strain chart, the reader is referred to Appendix A (Fig. A1).

ACCEPTED MANUSCRIPT

3.2. Additional transfer zone models (Series 2 and 3)

As the models of series 1 did not produce a single, continuous transfer zone, possibly because the total extension was not sufficient to do so (Acocella et al., 2005), we ran two additional model series with different set-ups (Table 2). The additional model series involve a secondary seed (representing a secondary structural grain to localize a transfer zone), rift segment underlap (angle φ = 75˚ and 25˚ for series 2 and 3 respectively) and oblique extension (angle α = 15˚ and -30˚ for series 2 and 3 respectively, Fig. 2e-g). These set-ups are similar to those tested by Zwaan and Schreurs (2017): the minor underlap and dextral transtension favours transfer zone formation by directing rift propagation towards the other rift segment in series 2, whereas the significant underlap combined with sinistral oblique extension produces a strike-slip dominated transfer zone in series 3.

3.2.1. Series 2 models

The series 2 models show the development of a continuous transfer zone basin with connected boundary faults between the rift segments, all situated above the secondary seed (Fig. 12). As previously observed in model series 1, syn-rift sedimentation does not significantly affect the large-scale structures so that rift segments as well as the transfer zone have a very similar geometry in both models. However, the structures within the rift segments and transfer zone are strongly influenced when syn-rift sedimentation is applied (Model J) or absent (Model I). Compared to Model I, Model J has a flatter rift topography, less faulting and more subsidence within the rift basin (Fig. 12i, j). Because the transfer zone consists of a continuous basin, flanked by oblique slip-normal faults, it behaves as an obliquely opening rift segment. The transfer zone shows a similar architecture to the main rift rift segments between which it is situated (Fig. 12i, j). In Model I the surface within the transfer zone basin is subsiding more as compared to the transfer zone basin in Model J. The transfer zone also experiences by more internal deformation structures, while the viscous layer has risen closer to the surface. However during the early model phases, both models show the innermost rift boundary faults connecting via a strike-slip fault within the developing transfer zone (Fig. 12b, b', f, f'). In later stages, this structure evolves in a series of right-stepping en-echelon faults (Fig. 12d, d', h, h'). As a result, the transfer zones have a much more complexly faulted appearance than the main rift segments.

ACCEPTED MANUSCRIPT

3.2.2. Series 3 models

Similar to the dextral oblique extension models of series 2, the sinistral oblique extension models of series 3 also form distinctive main rift segments and a transfer zone along the primary and secondary seeds, respectively (Fig. 13). Again, on a large scale the rift segments are not much affected by syn-rift sedimentation (Fig. 13d, d', h, h'), although internal structures are (Fig. 13i and j). Synkinematic sediments in Model N (Fig. 13, left column) results in a flatter rift topography, a less faulted rift structure and overall more subsidence than Model N without sedimentation (Fig. 13j).

The transfer zone initiates as a sinistral strike-slip zone in both models (Fig. 13b, b' and f, f'). Subsequently Model M develops a single large basin within the transfer zone, which has a right-stepping en-echelon arrangement with respect to the main rift segment (Fig. 13c, c'). In contrast, Model N develops a more fragmented structure with multiple small right-stepping basins in an en-echelon configuration (Fig. 13g, g'). Finally, in both models the transfer zone evolves into a continuous trough between rift-boundary faults (Fig. 13d, d', h, h', i and j), in which syn-rift sedimentation has a comparable effect on internal structures as in the main rift segments, although the latter are less faulted (Fig 13i, j).

ACCEPTED MANUSCRIPT

ACCEPTED MANUSCRIPT

4. Discussion

4.1. Large-scale rift and rift interaction zones

The overall evolution of rift segments and rift interaction zones as a function of extension obliquity in our models are similar to those described by Zwaan et al. (2016) and Zwaan and Schreurs (2017). Early rift segments develop above the seeds, revealing the important influence of structural weaknesses on the initial position of rift segments. The narrower and shallower rifts with steeper rift boundary faults that develop with increasing degrees of oblique extension (Fig. 8a-c) are logical, as the system becomes more strike-slip dominated. Furthermore, the development of en-echelon boundary faults and rift-internal structures (Fig. 3c) is a common feature in oblique extension settings (e.g. Tron and Brun, 1991; McClay and White, 1995; Morley et al., 2004) as extensional structures tend to develop approximately perpendicular to the extension direction (e.g. Hus et al., 2005).

The latter process also has a dominant influence on the rift interaction structures in our series 1 models. Orthogonal extension causes the rift segments to propagate roughly parallel to each other, while increasing degrees of dextral oblique extension promote linkage of right-stepping rift segments. This rule also holds for the opposite case: sinistral oblique extension in combination with left-stepping rift segments promotes rift linkage (Zwaan and Schreurs, 2017). However, the presence of secondary weaknesses results in a more complex evolution. In the series 2 models, the transfer zone is much more localized with respect to the rift pass structures forming in the series 1 models due to the presence of a rift-connecting seed (compare Fig. 7 and Fig. 12). Yet, the 15˚ dextral oblique extension in series 2 models also favours rift linkage since the general stress field induces the rifts to propagate toward each other. On the other hand, the series 3 set-up with 30˚ sinistral oblique extension could cause the propagating rifts to grow apart by the same principle. Though in these models, the seed localizes deformation, producing an initial sinistral strike-slip dominated transfer zone that evolves into a series of basins and finally forms a continuous trough (Fig. 13). However, Zwaan and Schreurs (2017) have noted that the same set-up without a rift-connecting seed may also produce a similar transfer zone due to local stress field modifications.

These general results are not significantly altered when we incorporate synkinematic sedimentation. Our models suggest that syn-rift sedimentation does not have a significant influence on the large-scale rift and transfer zone development within our model parameter space. This first-order observation is of importance for previous model studies with the same

ACCEPTED MANUSCRIPT

basic set-up but without sedimentation (e.g. Le Calvez and Vendeville, 2002; Zwaan et al., 2016; Zwaan and Schreurs, 2017), since it validates their large-scale model results.

4.2. Sedimentary loading and basin architecture

The large-scale rift setting might not be significantly affected by sedimentation, but a close-up view on the rift-internal structures shows that there are significant differences between models with and without sedimentation. The flat topography seen in syn-rift sedimentation models is a logical consequence of sedimentation (as we fill the rift basins to rift shoulder level). The other striking differences that occur when sedimentation is applied (less faulting within the rift wedge, higher subsidence and less uplift of the viscous lower crust) are due to the effects of sedimentary loading (Fig. 14b and b').

The influx of sediments causes an increased gravitational load on the rift wedge, which subsequently subsides deeper into the viscous layer below, simultaneously preventing the viscous material from rising (compare Model B with Model C, Figs. 9g-l, 11g-l). Sedimentary loading also affects the footwall segments of the rift boundary faults as Model C, including syn-rift sedimentation, shows a more pronounced subsidence of the footwall segments than observed in Model B without sedimentary loading (Figs. 9g-l, 11g-l). The infill and loading effects due to sedimentation also increase the strength of the sand and the shear zones with depth so that faulting is more localized and fault displacement increases (Fig. 14a, b), a feature also observed in previous numerical models (Olive et al., 2014). In contrast, a lack of sedimentation in the models thins and weakens the rift wedge, which is then easily deformed and broken up to spread over the widening gap (Fig. 14b), similar to the simulations of Burov and Poliakov (2001). Furthermore, the pronounced isostatic rise of the viscous lower crust (Figs. 9g-l, 10g-l) enhances internal rift wedge deformation, while hanging wall unloading supports relative rift shoulder uplift (Fig. 5a-d, i-l, Weissel and Karner, 1989).

Sedimentary infill also supports the stability of the rift shoulders so that rift boundary faults do not collapse and decrease fault dip angle as readily as in the models without sedimentation (Fig. 8d-f). However, this effect diminishes with increasing extension obliquity. Probably, the rift basin becomes more extension-dominated with progressing deformation, so that the initial steep rift boundary faults acquire an increasingly stronger dip-slip component and tilt towards the shallower fault angles typical for pure normal faults (Fig. 7b, o-z). The rise of the viscous layer below the rift may also cause rotation of the rift boundary faults.

ACCEPTED MANUSCRIPT

However, the role of syn-rift sedimentation during the evolution of a rift segment depends on the amount of accommodation space that is created over time. We observe the most significant influence of sedimentation in the main rift segments of our models, where most extension and subsidence is focused. These effects grow stronger towards the end of the model run, when most sediment loading has accumulated. In contrast, the impact of sedimentation is limited along the propagating rift branches from series 1 (Figs. 5-7), as these structures undergo much less subsidence during the model run. The models from series 2 and 3 (Figs. 12 and 13) do develop rift-dominated transfer zones, but these are less developed than the main rift segments. It follows that within our parameter space, syn-rift sedimentation has a minor effect on internal structuration of rift interaction zones and is most influential in the main rift segments and becomes more important with progressive rifting.

4.3. Oblique extension and strike-slip faulting

Another factor influencing the development of accommodation space is the degree of oblique extension. Our models indicate, in line with previous findings (e.g. Zwaan et al., 2016), that increasing degrees of oblique extension decrease basin widths, as rift boundary faults steepen due to the stronger strike-slip component (Fig. 8a). In combination with less subsidence in the rift basin, high degrees of oblique extension decrease the amount of accommodation space available (Fig. 8b) and thus repress the effects of syn-rift sedimentation. This is the case with Model H (60˚ dextral oblique extension, Fig. 4c and f), which did not produce enough accommodation space during the early stages to apply sedimentation. Model N provides another example (Fig. 13), in which a strike-slip zone establishes the earliest rift connection, allowing little sedimentary infill during the initial phases. This is a specific model with a specific set-up, but transfer fault zones connecting rift segments are often observed in nature (e.g. Morley et al., 2004, Fig. 1d) and are probably little affected by synkinematic sedimentation. However, in the Model N case, the transfer fault does subsequently develop into a rift basin, similar to the Rukwa Basin in the Tanganyika-Rukwa-Malawi fault zone in East Africa (Rosendahl et al., 1992; Chorowicz, 2005; Zwaan and Schreurs, 2017). Thus, an initial strike-slip transfer fault system can in later stages evolve into a rift-type sediment-filled basin.

4.4. Basin architecture: model vs nature

Although sedimentation is shown not to have a strong effect on initial rift and rift interaction structures, it has significant influence on rift-internal structures. We often find thick sedimentary infill within rift basins, for instance in the Rhine Graben, (Derer et al., 2005), East African Rift System (Morley, 1988; Ebinger, 1989), North Sea (Erratt et al., 1999) and

ACCEPTED MANUSCRIPT

Baikal Rift (Hutchinson et al., 1992; Hus et al., 2012). The curved rift valley floor topography seen in our models without sedimentation is rather unlike the geometries observed in young continental rift settings, as is the model basin depth of ca. 10 mm, which translates to ca. 5 km or more in nature; the deepest continental rift basin, Lake Baikal, is 1,600 m deep (Hutchinson et al., 1992) and even the mean ocean depth on Earth only amounts to some 3.7 km (Charette and Smith, 2010). Although our crustal scale sedimentation experiments do not capture factors as lithospheric flexure and isostasy or mantle upwelling, which might mitigate the degree of subsidence, they provide a more realistic rift geometry and topography. It is therefore desirable to apply (at least a degree of) sedimentation when modelling extensional tectonics.

4.5. Rift pass structures

The propagating rift tips in the models from series 1 lead to the formation of a horst or rift pass structure between both rift segments that can eventually lead to microcontinent formation (Nelson et al., 1992; Koehn et al. 2008), especially in oblique extension conditions (Figs. 4-7). DVC analysis demonstrates that the relative uplift of the central horst or rift pass block, within a regionally subsiding area, is due to hanging wall unloading as a result of rift activity on both sides (Figs. 9g-l, 11g-l). Furthermore, the slight rotation of the rift pass block is a logical result of the extension gradient along the propagating rift segments (Figs. 4a, 9j-l, 11j-l, 15a). This extension gradient also causes the flow of viscous material towards the most developed part of the rift, where the strongest isostatic compensation occurs (Figs. 9, 11, 15b).

Similar structural highs as those in our experiments occur in the North Sea Central Graben, situated between Late Jurassic-Early Cretaceous left-stepping rift segments (Fig. 16) that opened along pre-existing tectonic lineaments inherited from the Caledonian orogeny (Bartholomew et al., 1993). A first rift phase in the Triassic formed the rough Central Graben structure was reactivated during subsequent Late Jurassic-Early Cretaceous extension, probably under orthogonal or near-orthogonal extension conditions (Erratt et al., 1999, 2010). While deep rift basins formed during these rifting events, leading to the deposition of world-class Upper Jurassic hydrocarbon source rocks (Gautier, 2005), the intervening highs remained emergent and subjected to erosion. The highs were only flooded following regional post-rift thermal subsidence initiated in Late Cretaceous times, occasionally interrupted by local pulses of inversion that continued into the Cenozoic (Cartwright, 1989; Johnson et al., 2005).

ACCEPTED MANUSCRIPT

An excellent example of such a rift pass block is the Mandal High at the Norwegian-Danish Border, situated between the Feda Graben in the west and the Søgne Basin in the east (Fig. 17). It remained a stable and exposed structural high from Permian times until the Late Cretaceous, while the adjacent Feda Graben and Søgne Basin experienced significant amounts of tectonic subsidence and sediment infill during the two major rift phases (Fig. 17b, c,). Note the effect of the Upper Permian (Zechstein) evaporites on the structural style. Post-rift thermal sag resulted in the deposition of thick layers of chalk sediments (Surlyk et al., 2003), that are slightly deformed due to Late Cretaceous-Cenozoic inversion and associated salt motion (diapirism). The whole structure is nowadays overlain by several kilometres of Cenozoic infill (Fig. 17e).

4.6. Additional insights from DVC analysis

Although CT scanning provides a very useful non-destructive method to monitor the internal 3D structural evolution of our models, the CT-images themselves only allow a predominantly qualitative structural analysis (Figs. 6-8, 12-13). With the use of DVC analysis, we can now for the first time reveal and quantify the complex 3D displacement and strain patterns occurring in both the brittle and viscous parts of our models (Figs. 9-11). The results indicate the clear distinctions between brittle and viscous behaviour, where deformation is either strongly localized or distributed (Fig. 10). Especially the distributed deformation within the viscous layer is demonstrated to be complex (Figs. 10g-l). Furthermore, the relatively minor boundary effects near the sides of the models (best visible on Fig. 9a-f and 10g-i) are shown to influence material flux in the viscous layer. The 3D aspect of the DVC analysis also illustrates the flow of viscous material out of section in orthogonal extension models and the rotation of the rigid rift pass block about a vertical axis (Figs. 9j-l, 10j-l, 15). Therefore, a simple 2D crustal-scale restoration of an orthogonal extended rift system could be flawed if such effects are not taken into account.

Altogether, DVC analysis of CT data allows a much more thorough and detailed understanding of our models and the possibility to map small distributed and large localized deformation and displacements could be a powerful tool for analogue-numerical comparison and calibration.

4.7. Implications for continental break-up

Our models demonstrate that syn-rift sedimentation does not have an important influence on early large-scale rift and rift interaction zone development. Yet, sedimentation might be of importance on a longer timescale. We see how models without sedimentation develop a strongly thinned upper crust, which can be expected to break apart when further extension

ACCEPTED MANUSCRIPT

occurs. On the other hand, constant infill of the rift basin could constantly strengthen the upper crust and potentially prevent any break-up from occurring (Fig. 14c'). The amounts of material needed for the latter scenario are rather enormous and therefore unlikely to be available, but a steady influx of sediment could significantly delay continental break-up, as seen in the Gulf of California (Martín-Barajas et al., 2013). In contrast, a low sediment supply leading to starved basins is quite common (e.g. the Jurassic North Sea rifts, Fraser et al., 2003) facilitating continental break-up (Fig. 14c).

However, the processes associated with rifting and eventual break-up are numerous. For instance the lithospheric strength profile and the degree of brittle-ductile coupling within the system has a strong influence on fault localization and the style of rifting (e.g. Dunbar and Sawyer, 1998; Brun, 1999; Buiter et al., 2008). Isostatic compensation and flexure on a lithospheric scale as well as mantel plume emplacement commonly modifies rift zone topography significantly (Weissel and Karner, 1989; Underhill and Partington, 1993; Moucha and Fore, 2011). Mantle plume-induced thermal variations also influence the lithospheric strength profile and the associated magmatism and intrusion (i.e. diking) are known to promote break-up (Buck, 2004; Ebinger 2012). The thickness of the lithosphere (e.g. cratonic roots) directs the flow of mantle plume material and thermal variations (Fouch et al., 2000). Another thermal effect may occur during pauses in rift activity, causing cooling and strengthening of the risen asthenosphere below the rift so that with renewed extension, rifting may initiate elsewhere (Naliboff and Buiter, 2015).

As a matter of fact, most rifts fail to split a continent, emphasizing that continental break-up is a complex process (Ebinger, 2012). Although syn-sedimentary loading may influence the process, we should consider it in the larger context of the complete extensional system and the larger-scale processes mentioned above, which determine the long-term rift evolution. These processes are however not included in our crustal-scale analogue models. Lithospheric-scale analogue models involving syn-sedimentation would allow a better constraint on the mechanical behaviour of the system (lithospheric flexure, isostasy), whereas numerical models would enable the simulation of chemical and thermal influences.

ACCEPTED MANUSCRIPT

5. Conclusion

We conducted various crustal-scale analogue tectonic models to investigate the effects of syn-rift sedimentation on rift and rift interaction zone development in continental settings and come to the following conclusions:

- On a large scale, syn-rift sedimentation does not significantly influence the development of rift and rift interaction structures;
- Syn-rift sedimentation can however strongly affect rift-internal structures: sedimentary loading reinforces the rift wedge, decreasing rift wedge faulting, and increasing subsidence of the rift wedge;
- These effects are strongest in areas where most accommodation space is available, that is, along the main rift segments. In contrast, rift segments that undergo high degrees of oblique extension develop less accommodation space and can be expected to be significantly less affected by sedimentary loading;
- Rift interaction structures in our parameter space are least affected by sediment influx, as they undergo relatively low amounts of subsidence so that little accommodation space is available;
- We advise to apply sedimentation in models of extensional tectonic settings, as our rift basins with syn-rift sedimentation develop more realistic features than the models without;
- Novel 3D DVC analysis allows a much more thorough understanding of our models than surface images or CT scans alone can provide. It enables the highly detailed monitoring and quantification of material displacement and deformation, revealing the complex behaviour of the opaque brittle and viscous model materials;.
- The 3D DVC analysis demonstrates that material can move out of plane in orthogonal extension settings due to viscous flow or block rotation about a vertical axis, which has to be taken in account when conducting structural reconstructions;
- The above conclusions are valid for the early stages of rift development, when a high sediment influx could delay continental break-up. However, the long-term evolution of the rift system is dominated by other, lithospheric-scale processes.

ACCEPTED MANUSCRIPT

6. Acknowledgements

We would like to express our gratitude to Nicole Schwendener for assisting us with the CT-scanning, Marco Herwegh for providing funds to upgrade the experimental apparatus and to the engineers from IPEK Rapperswil (Theodor Wüst, Reto Gwerder, Rudolf Kamber, Michael Ziltener and Christoph Zolliker) for realizing these improvements. We would also like to thank Carlo Bernasconi AG for providing us with a free parcel of Zirschot, and Dave Hollis (LaVision UK) for help with CT data import in Davis and DVC software support. The tomographic DVC technical equipment of the Fault Dynamics Research Group at Royal Holloway University of London was supported by industry partners of the STAR consortium (Structural Analogues of Reservoirs). We would also like to thank David Boutelier and Nicolas Molnar for their helpful and constructive reviews. This project was supported by the Swiss National Science Foundation (grant no. 200021_147046/1)

7. Appendix

__FIG APPENDIX 1_

8. References

Acocella, V., Faccenna, C., Funiciello, R., Rossetti, F., 1999a. Sand-box modelling of basement-controlled transfer zones in extensional domains. Terra Nova 11 (4), 149-156. doi: 10.1046/j.1365-3121.1999.00238.x

Acocella, V., Salvini, F., Funiciello, R., Facenna, C., 1999b. The role of transfer structures on volcanic activity at Campi Flegrei (Southern Italy). J. Volcanol. Geoth. Res. 91, 123–139. https://doi.org/10.1016/S0377-0273(99)00032-3

Acocella, V., Morvillo, P., Funiciello, R., 2005. What controls relay ramps and transfer faults within rift zones? Insights from analogue models. J. Struct. Geol. 27, 397-408. doi: 10.1016/j.jsg.2004.11.006

Adam, J., Urai, J.L., Wieneke, B., Oncken, O., Pfeiffer, K., Kukowski, N., Lohrmann, J., Hoth, S., van der Zee, W., Schmatz, J., 2005. Shear localisation and strain distribution during tectonic faulting - new insights from granular-flow experiments and high-resolution optical

ACCEPTED MANUSCRIPT

image correlation techniques. J. Struct. Geol. 27, 2, 283-301. doi: http://dx.doi.org/10.1016/j.jsg.2004.08.008

Adam, J., Klinkmüller, M., Schreurrs, G., Wieneke, B., 2013. Quantitative 3D strain analysis in analogue experiments simulating tectonic deformation: Integration of X-ray computed tomography and digital volume correlation techniques. J. Struct. Geol. 55, 127-149. doi: http://dx.doi.org/10.1016/j.jsg.2013.07.011

Allken, V., Huismans, R.S., Thieulot, C., 2011. Three-dimensional numerical modeling of upper crustal extensional systems. J. Geophys. Res. 116, B10409. doi: 10.1029/2011JB008319

Allken, V., Huismans, R.S., Thieulot, C., 2012. Factors controlling the mode of rift interaction in brittle-ductile coupled systems: A 3D numerical study. Geochem. Geophys. Geosyst. 13 Q05010. doi: 10.1029/2012GC004077

Basile, C., Brun, J.-P., 1999. Transtensional faulting patterns ranging from pull-apart basins to transform continental margins: an experimental investigation. J. Struct. Geol. 21, 23-37. doi: 10.1016/S0191-8141(98)00094-7

Bialas, R. W., Buck., W. R., 2009. How sediment promotes narrow rifting: Applications to the Gulf of California. Tectonics, 28, TC4014. doi: 10.1029/2008TC002394

Blair, T.C., Bilodeau, W.L., 1998. Development of tectonic cyclothems in rift-pull-apart, and foreland basins: Sedimentary response to episodic tectonism. Geology, 16, 517-520. doi: https://doi.org/10.1130/0091-7613(1988)016<0517:DOTCIR>2.3.CO;2

Boutelier, D., Oncken, O., Cruden, A., 2012. Fore-arc deformation at the transition between collision and subduction: Insights from 3-D thermomechanical laboratory experiments. Tectonics 31, TC2015. doi:10.1029/2011TC003060,

Brun, J-.P., 1999. Narrow rifts versus wide rifts: inferences for the mechanics of rifting from laboratory experiments. Philos. Trans. Roy. Soc. London 357, 695-712. doi: 10.1098/rsta.1999.0349

ACCEPTED MANUSCRIPT

Brun, J-P, Fort, X., 2008. Entre sel et terre. Structures et mécanismes de la tectonique salifère. Collection Interactions, Vuibert, Paris.

Brune, S., Popov, A.A., Sobolev, S.V., 2012. Modeling suggests that oblique extension facilitates rifting and continental break-up. J. Geophys. Res.117, B08492. doi: 10.1029/2011JB008860

Buck, W.R., 1991. Models of Continental Lithospheric Extension. J. Geophys. Res. 96, 20,161-20,178. doi: 10.1029/91JB01485

Buck, W.R., 2004. Consequences of Asthenospheric Variability on Continental Rifting. In: Karner, G., Taylor, B., Driscoll, N., Kohlstedt, B. (eds) Rheology and Deformation of the Lithosphere at Continental Margins. Columbia University Press, New York, 92–137.
No doi available

Buiter, S.J.H., Huismans, R.S., Beaumont, C., 2008. Dissipation analysis as a guide to mode selection during crustal extension and implications for the styles of sedimentary basins. J. Geophys. Res. 113, B06406. doi: 10.1029/2007JB005272

Burov, E., Poliakov, A., 2001. Erosion and rheology controls on synrift and postrift evolution: Verifying old and new ideas using a fully coupled numerical model. J. Geophys. Res. 106 (B8), 16,461-16,481. doi: 10.1029/2001JB000433

Carlo AG (Carlo Bernasconi AG, Switzerland), 2017. Company website http://www.carloag.ch/shop/mineralische-rohstoffe/strahlmittel/glas-und-keramik-strahlmittel/zirshot-z150-0-150-mm-0-210-mm.html

Cartwright, J.A., 1989. The kinematics of inversion in the Danish Central Graben. In: Cooper, M.A., Williams, G.D. (eds) Inversion Tectonics. Geol. Soc. Spec. Publ. 44, 153–175. DOI: 10.1144/GSL.SP.1989.044.01.10

Charette, M. A., Smith, W.H.F., 2010. The Volume of Earth's Ocean. Oceanogr. 23 (2), 112-114. doi: http://dx.doi.org/10.5670/oceanog.2010.51

Corti, G., 2012. Evolution and characteristics of continental rifting: Analog modeling-inspired view and comparison with examples from the East African Rift System. Tectonophysics 522-523, 1-33. doi: 10.1016/j.tecto.2011.06.010

ACCEPTED MANUSCRIPT

Corti, G., Bonini, M., Sokoutis, D., Innocenti, F., Manetti, P., Cloetingh, S., Mulugeta, G., 2004. Continental rift architecture and patterns of magma migration: A dynamic analysis based on centrifuge models. Tectonics 23, TC2012. doi: 10.1029/2003TC001561

Derer, C.E., Schumacher, M.E., Schäfer, A., 2005. The northern Upper Rhine Graben: basin geometry and early syn-rift tectono-stratigraphic evolution. Int. J. Earth. Sci. (Geol. Rundschau) 94, 640-656. DOI: 10.1007/s00531-005-0515-y

Dunbar, J.A., Sawyer, D.S., 1989. How Preexisting Weaknesses Control the Style of Continental Breakup. J. Geophys. Res 94, B6, 7278-7292. doi: 10.1029/JB094iB06p07278

Ebinger, C.J., 1989. Tectonic development of the western branch of the East African rift system. Geol. Soc. Am. Bull. 101, 885-903. doi: 10.1130/0016-7606(1989)101<0885:TDOTWB>2.3.CO;2

Ebinger, C.J., 2012. Evolution of the Cenozoic East African rift system: Cratons, plumes, and continental break-up. In: Roberts, D. G., Bally, A. W. (eds) Regional Geology and Tectonics: Phanerozoic Rift Systems and Sedimentary Basins, 1B, 132-162. http://dx.doi.org/10.1016/B978-0-444-56356-9.00006-7

Elmohandes, S-.E., 1981. The Central European Graben System: Rifting Imitated by Clay Modelling. Tectonophysics 73, 69-78. doi: 10.1016/0040-1951(81)90174-8

Erratt, D., Thomas, G. M., Wall, G. R. T., 1999. The evolution of the Central North Sea Rift, Petrol. Geol. Conference Series 5, pp 63-82

Erratt, D., Thomas, G.M., Hartley, N.R., Musum, R., Nicholson, P.H., Spisto, Y., 2010. North Sea hydrocarbon systems: some aspects of our evolving insights into a classic hydrocarbon province. In: Vining, B. A., Pickering, S. C. (eds) Petroleum Geology: From Mature Basins to New Frontiers – Proceedings of the 7th Petroleum Geology Conference, 37–56. doi: 10.1144/0070037

Faulds, J.E., Varga, R.J., 1998. The role of accommodation zones and transfer zones in the regional segmentation of extended terranes. In: Faulds, J.E., Stewart, J.H. (eds) Accommodation Zones and Transfer Zones: The Regional Segmentation of the Basin and

ACCEPTED MANUSCRIPT

Range Province. Geol. Soc. Am. Spec. Paper 323, pp. 1-46. doi: 10.1130/0-8137-2323-X.1

Fossen, H., Schultz, R.A., Rundhovde, E., Rotevatn, A., Buckley, S.J., 2010. Fault linkage and graben stepovers in the Canyonlands (Utah) and the North Sea Viking Graben, with implications for hydrocarbon migration and accumulation. AAPG Bull. 94 (5), 597-613. doi: 10.1306/10130909088

Fouch, M.J., Fischer, K.M., Parmentier, E.M., Wysession, M.E., Clarke, T.J., 2000. Shear wave splitting, continental keels, and patterns of mantle flow. J. Geophys. Res. 105, B3, 6255-6275. doi: 10.1029/1999JB900372

Fraser, S., Robinson, A., Johnson, H., Underhill, J., Kadolsky, D., 2003. Upper Jurassic. In: Evans, D., Graham, C., Armour, A., Bathurst, P. (eds) 2003. The Millennium Atlas: Petroleum Geology of the Central and Northern North Sea. Geol. Soc. London, 155-189

Gautier, D.L., 2005. Kimmeridge Shales Total Petroleum System of the North Sea Graben Province. U.S. Geol. Survey Bull. 2204-C. https://pubs.usgs.gov/bul/2204/c/pdf/B2204C.pdf

Gray, R., Pysklywec, R.N., 2012. Influence of sediment deposition on deep lithospheric tectonics. Geophys. Res. Lett. 39, L11312. doi:10.1029/2012GL051947

Hubbert, M.K., 1937. Theory of scaled models as applied to the study of geological structures. Geol. Soc. Am. Bull. 48, 1459-1520. doi: 10.1130/GSAB-48-1459

Hus, R., Acocella, V., Funiciello, R., De Batist, M., 2005. Sandbox models of relay ramp structure and evolution. J. Struct. Geol. 27, 459-473. doi:10.1016/j.jsg.2004.09.004

Hus, R., Poort, J., Charlet, F., Naudts, L., Khlystov, O., Klerkx, J., De Batist, M., 2012. Lake Baikal. In: Roberts, D. G., Bally, A. W. (eds) Regional Geology and Tectonics: Phanerozoic Rift Systems and Sedimentary Basins, 1B, 258-276. http://dx.doi.org/10.1016/B978-0-444-56356-9.00010-9

Hutchinson, D.R., Golmshtok, A.J., Zonenshain, L.P., Moore, T.C., Scholz, C.A., Klitgord, K.D., 1992. Depositional and tectonic framework of the rift basins of Lake Baikal from

ACCEPTED MANUSCRIPT

multichannel seismic data. Geology 20, 589-592. doi: 10.1130/0091-7613(1992)020<0589:DATFOT>2.3.CO;2

Johnson, J., Lott, G.K., 1993. 2. Cretaceous of the Central and Northern North Sea. In: Knox, R.W.O'B., Cordey, W.G. (eds) Lithostratigraphic nomenclature of the UK North Sea. British Geological Survey (Nottingham).

Klinkmüller, M., 2011. Properties of analogue materials, experimental reproducibility and 2D/3D deformation quantification techniques in analogue modeling of crustal-scale processes. Unpublished PhD Thesis, University of Bern, Switzerland.

Koehn, D., Aanyu, K., Haines, S., Sachau, T., 2008. Rift nucleation, rift propagation and the creation of basement micro-plates within active rifts. Tectonophysics 458, 105-116. doi:10.1016/j.tecto.2007.10.003Larsen, P-.H., 1988. Relay structures in a Lower Permian basement-involved extension system, East Greenland. J. Struct. Geol. 10, 3-8. doi: 10.1016/0191-8141(88)90122-8

Lambiase, J.J., Bosworth, W., 1995. Structural controls on sedimentation in continental rifts. In: Lambiase, J.J. (ed) Hydrocarbon Habitat in Rift Basins. Geol. Soc. London Spec. Publ. 80, 117-133.

Le Calvez, J.H., Vendeville, B.C., 2002. Experimental designs to model along-strike fault interaction. In: Schellart, W.P., Passchier, C. (eds) Analogue modelling of large-scale tectonic processes. J. Virt. Expl. 7, 1-17. doi: 10.3809/jvirtex.2002.00043

Lohrmann, J., Kukowski, N., Adam, J., Oncken, O., 2003. The impact of analogue material properties on the geometry, kinematics, and dynamics of convergent sand wedges. J. Struct. Geol. 25, 1691-1711. doi: 10.1016/S0191-8141(03)00005-1

Liu, L., Morgan, E.F., 2007. Accuracy and Precision of Digital Volume Correlation in Quantifying Displacements and Strains in Trabecular Bone. J. Biomech. 40, 3516-3520. https://doi.org/10.1016/j.jbiomech.2007.04.019

Madi, K., Tozzi, G., Zhang, Q.H., Tong, J., Cossey, A., Au, A., Hollis, D., Hild, F., 2013. Computation of full-field displacements in a scaffold implant using digital volume correlation and finite element analysis. Med. Eng. Phys. 35 (9), 1298-1312. http://dx.doi.org/10.1016/j.medengphy.2013.02.001

ACCEPTED MANUSCRIPT

show

Martins-Neto, M.A., Catuneanu, O., 2012. Roberts, D.G., Bally, A.W. Rift sequence stratigraphy. In: Roberts, D.G., Bally, A.W. (eds) Regional Geology and Tectonics: Phanerozoic Rift Systems and Sedimentary Basins, 1B, 58-70. http://dx.doi.org/10.1016/B978-0-444-56356-9.00003-1

McClay, K.R., White, M.J., 1995. Analogue modelling of orthogonal and oblique rifting. Mar. Petrol. Geol. 12, 137-151. doi: https://doi.org/10.1016/0264-8172(95)92835-K

Morley, C.K., 1988. Variable extension in Lake Tanganyika. Tectonics, 7, No. 4, 785-801. doi: 10.1029/TC007i004p00785

Morley, C.K., Nelson, R.A., Patton, T.L., Munn, S.G., 1990. Transfer zones in the East African Rift System and their relevance to hydrocarbon exploration in rifts. AAPG Bull. 74, 1234-1253. No doi available

Morley, C.K., Haranya, C., Phoosongsee, W., Pongwapee, S., Kornsawan, A., Wonganan, N., 2004. Activation of rift oblique and rift parallel pre-existing fabrics during extension and their effect on deformation style: examples from the rifts of Thailand. J. Struct. Geol. 26, 1803-1829. doi: 10.1016/j.jsg.2004.02.014

Moucha, R., Forte, A.M., 2011. Changes in African topography driven by mantle convection. Nat. Geosci. 4, 707-712. doi: 10.1038/NGEO1235

Mulugeta, G., 1988. Squeeze box in the centrifuge. Tectonophysics 148, 323-335. doi: 10.1016/0040-1951(88)90139-4

Naliboff, J., Buiter, S.J.H., 2015. Rift reactivation and migration during multiphase extension. Earth Planet. Sci. Lett. 421, 58–67. http://dx.doi.org/10.1016/j.epsl.2015.03.050

Nelson, R.A., Patton, T.L., Morley, C.K., 1992. Rift-Segment Interaction and Its Relation to Hydrocarbon Exploration in Continental Rift Systems. AAPG Bull. 76, 1153-1169. No doi available

Olive, Behn, M.D., Malatesta, L.C., 2014. Modes of extensional faulting controlled by surface processes. Geophys. Res. Lett. 41, 6725-6733. doi:10.1002/ 2014GL061507

ACCEPTED MANUSCRIPT

Panien, M., Schreurs, G, Pfiffner, A., 2006. Mechanical behaviour of granular materials used in analogue modelling: insights from grain characterisation, ring-shear tests and analogue experiments. J. Struct. Geol. 28, 1710-1724. doi: 10.1016/j.jsg.2006.05.004

Pannier, Y., Lenoir, N., Bornert, M., 2010. Discrete volumetric digital image correlation for the investigation of granular type media at microscale: accuracy assessment. EPJ Web of Conferences 6, 35003. https://doi.org/10.1051/epjconf/20100635003

Paul, D., Mitra, S., 2013. Experimental models of transfer zones in rift systems. AAPG Bull. 97 (5), 759-780. doi: 10.1306/10161212105

Ramberg, H., 1981. Gravity, Deformation and the Earth's Crust. Academic Press, London.

Roberts, A.M., Price, J.D., Olsen, T.S., 1990. Late Jurassic half-graben control on the siting and structure of hydrocarbon accumulations: UK/Norwegian Central Graben. Geol. Soc. Spec. Publ. 55, 229-257. doi: 10.1144/GSL.SP.1990.055.01.11

Rosendahl, B.R., 1987. Architecture of Continental Rifts with Special Reference to East Africa. Annu. Rev. Earth Planet. Sci. 15, 445-503. doi: 10.1146/annurev.ea.15.050187.002305

Rosendahl, B.R., Kilembe, E., Kaczmarick, K., 1992. Comparison of the Tanganyika, Malawi, Rukwa and Turkana Rift zones from analyses of seismic reflection data. Tectonophysics, 213, 235-256. doi: https://doi.org/10.1016/0040-1951(92)90261-4

Saria, E., Calais, E., Stamps, D.S., Delvaux, D., Hartnady, C.J.H., 2014. Present-day kinematics of the East African Rift. J. Geophys. Res. Solid Earth 119, 3584-3600. doi:10.1002/2013JB010901.

Scholz, C.A., Hutchinson, D.R., 2000. Stratigraphic and structural evolution of the Selenga Delta Accommodation Zone, Lake Baikal Rift, Siberia. Int. J. Earth Sci 89, 212-228. doi: 10.1007/s005310000095

Simpson, G., 2006. Dynamic interactions between erosion, deposition, and three-dimensional deformation in compressional fold belt settings. J. Geophys. Res 109, F03007. doi:10.1029/2003JF000111

ACCEPTED MANUSCRIPT

Stolar, D., Roe, G., Willet, s., 2007. Controls on the patterns of topography and erosion rate in a critical orogen. J. Geophys. Res 112, F04002. doi:10.1029/2006JF000713

Strak, V., Schellart, W.P., 2014. Evolution of 3-D subduction-induced mantle flow around lateral slab edges in analogue models of free subduction analysed by stereoscopic particle image velocimetry technique. Earth Planet. Sci. Lett. 403, 368–379. http://dx.doi.org/10.1016/j.epsl.2014.07.007

Surlyk, F., Dons, T., Clausen, C. K., Higham, J. 2003. Upper Cretaceous. In: Evans, D., Graham, C., Armour, A., Bathurst, P. (eds) The Millennium Atlas: Petroleum Geology of the Central and Northern North Sea. Geol. Soc. London, 213–233.
No doi available

Thomas, E., Diapirisme salifère induit par l'extension. Mém. DEA, Université de Rennes 1, 102p.

Underhill, J.R., Partington, M.A. 1993. Jurassic thermal doming and deflation in the North Sea: implications of the sequence stratigraphic evidence. In: Parker, J.R. (ed) Petroleum Geology: North-West Europe and Global Perspectives - Proceedings of the 4th Petroleum Geology Conference. Geol. Soc. Petrol. Geol. Conf. Series, 4, 337–345. DOI: 10.1144/0040337

Ustaszewski, K., Schumacher, M.E., Schmid, S.M., Nieuwland, D., 2005. Fault reactivation in brittle-viscous wrench system-dynamically scaled analogue models and application to the Rhine-Bresse transfer zone. Quat. Sci. Rev. 24, 365-382. doi: 10.1016/j.quascirev.2004.03.015

Weijermars, R., Schmeling, H., 1986. Scaling of Newtonian and non-Newtonian fluid dynamics without inertia for quantitative modelling of rock flow due to gravity (including the concept of rheological similarity). Phys. Earth Planet. Inter. 43, 316-330. doi: 10.1016/0031-9201(86)90021-X

Weissel, J.K., Karner, G.D., 1989. Flexural uplift of rift flanks due to mechanical unloading of the lithosphere during extension. J. Geophys. Res. 94, B10, pp. 13,919-13,950. DOI: 10.1029/JB094iB10p13919

ACCEPTED MANUSCRIPT

Zwaan, F., Schreurs, G., Naliboff, J., Buiter, S.J.H., 2016. Insights into the effects of oblique extension on continental rift interaction from 3D analogue and numerical models. Tectonophysics 693, pp. 239-260. doi: http://dx.doi.org/10.1016/j.tecto.2016.02.036

Zwaan, F., Schreurs, G., 2017. How oblique extension and structural inheritance influence rift segment interaction: Insights from 4D analog models. Interpretation 5 (1), SD119-SD138. doi: http://dx.doi.org/10.1190/INT-2016-0063.1

ACCEPTED MANUSCRIPT

ACCEPTED MANUSCRIPT

Table Captions

Table 1. Material properties.

Table 2. Summary of analogue model characteristics.

Table 3. Parameters used for model scaling.

ACCEPTED MANUSCRIPT

ACCEPTED MANUSCRIPT

Figure Captions

Figure 1.
Natural examples of rift interaction structures and accommodation/transfer zone convention: (a) Rift segments and distribution of sedimentary basins and volcanics in the East African Rift System. Image modified after Ebinger (1989) and Acocella et al. (1999a); (b) Western branch of the East African Rift System with major rift interaction zones with associated sediments and volcanics (modified after Corti, 2012), as well as current extension directions and velocities (modified after Saria et al. (2014). Location and names are shown in (a). Hatched faults represent normal faults, the character of faults without motion indications are not specified in the original publications; (c-d) Block diagrams depicting the differences between accommodation and transfer zones as proposed by Faulds and Varga (1998). (c) Accommodation zones (soft linkage) in which rift boundary faults do not connect, but die out laterally and overlap. Examples are found in the East African Rift System (b). (d) Transfer zones (hard linkage) in which the rift boundary faults are continuous from rift to rift, e.g. the Selenga Accommodation Zone in Lake Baikal (Scholz and Hutchinson, 2000) or in which a single transfer fault connects both basins, e.g. the Gulf of Suez or Thailand (Acocella et al., 1999a; Morley et al., 2004). Modified after Zwaan et al., 2016.

Figure 2.
Model set-up. (a) Cut-out view of the experimental apparatus depicting its various components. (b) Experimental apparatus in the CT-scanner during a model run. (c) Compositional layering of quartz and corundum sand representing the brittle upper crust and a viscous silicone/corundum sand mixture reproducing the ductile lower crust, overlying a foam base. (d-f) Schematic surface view showing the initial state (d) and subsequent deformation of the empty apparatus (e) orthogonal extension and (f) oblique extension, respectively. (g) Distribution of basal deformation in the model. As the sidewalls move apart with 7.5 mm/h, a velocity gradient develops in the foam and plexiglass base (yellow arrows). The darker x-shape in the image is a CT-artefact that appears in all CT-sections. CT-image derived from model G.

ACCEPTED MANUSCRIPT

Figure 2 (continued)

(h-j) Seed geometry set-up for our three model series in map view. (k) Extension obliquity definition for our models. (l) sediment application as seen on CT images. Left: rift basin opens after 60 min. Right: the basin is filled to model syn-rift sedimentation. (m) Example of a model run (Model G). Left: initial set-up top view (without sand cover to show the seed geometry). Middle: surface structures after 60 min. Right: basins are filled to model syn-rift sedimentation.

Figure 3.

Analysis of CT scanned analogue experiment using Digital Volume Correlation (DVC) techniques. (a) Voxel data of time-series experiment scans are subdivided into sub-volumes (Model B example). (b) Pattern search by cross-correlation of sub-volumes in reference and deformed volume yields the spatial average displacement (3D displacement vector) over the size of the sub-volume. (c) Pattern correlation with Fast Fourier Transformation (FFT) cross correlation function does not require tracking single particles. (d-d') CT sections from Model B used for DVC analysis. Intensity variations due to Zirshot ceramic beads in the brittle and viscous layers produce a random 3D image texture (i.e. marker particle pattern), necessary for DVC analysis. The image is optimized by stacking multiple CT sections, which reduces noise. (e) Finite displacement vectors (projected in xy-section) with colour map of horizontal displacement component (v_x); (f) Finite displacement vectors with colour map of longitudinal strain along the x-axis (e_{xx}) showing contraction and extension (cold and warm colours, respectively). Modified after Adam et al. (2013).

Figure 4.

Top view analysis of series 1 (Models B, C, F, H, and G), illustrating the influence of extension obliquity on transfer zone formation. Removing the sand cover reveals the deformation at the top of the viscous layer. Lighting directions are indicated to the left of each model.

Figure 5

3D CT-derived topography evolution of Models B, C, F and G (series 1). Brighter colours on the model surface represent higher parts of the model, which are therefore more transparent for X-rays and show up as a lighter colour. This provides a qualitative insight into vertical displacement.

ACCEPTED MANUSCRIPT

Figure 6.

CT-derived sections illustrating the internal structure and evolution of orthogonal extension Models B and C (series 1). Location of sections is shown in Fig. 5. Insets: grey represents the viscous layer, light yellow the sand and the red/light yellow alterations the syn-rift sediments.

Figure 7.

CT-derived sections illustrating the internal structure and evolution of 30˚ oblique extension Models F and G (series 1). Location of sections is shown in Fig. 5. Insets: grey represents the viscous layer, light yellow the sand and the red/light yellow alterations the syn-rift sediments.

Figure 8

Measurements on models, showing the influence of extension obliquity (angle α) and sedimentation on rift geometry. (a) Rift width, decreases with increasing extension obliquity and is consistently lower in models with sedimentation; (b) Subsidence (height difference between rift shoulders and rift valley floor; for models with sedimentation the height difference between rift shoulders and the base of the oldest sediments is measured), decreases with increasing extension obliquity and is consistently higher with sedimentation; (c) Initial boundary fault angle, which increases with higher extension obliquity (d) Final rift boundary angle, which is stable in models with sedimentation, but increases with higher extension obliquity; (e) change in rift boundary fault angle with time for models without sedimentation; (f) change in rift boundary fault angle for models with sedimentation.

Figure 9

DVC total displacement analysis of Model B (orthogonal extension, no sedimentation). (a-c) 3D displacement; (d-f) Horizontal displacement in the xy-plane, parallel to the extension direction. Warm colours represent displacement to the right, cold colours represent displacement to the left; (g-i) Vertical velocities. Warm colours represent upward displacement, cold colours represent downward displacement; (j-l) Horizontal velocities in the xz-plane (normal to section and extension direction). Warm colours represent displacement towards the observer, cold colours represent displacement away from the observer. The locations of sections I, II and III are close to those of sections 3, 4 and 6 in Figs. 5d and 6a.

ACCEPTED MANUSCRIPT

Figure 10

Strain charts of xy-sections derived from finite 3D strain fields of Model B (orthogonal extension, no sedimentation) obtained through DVC analysis. (a-c) 3D shear strain (positive values only): Higher values show more deformed areas (localised shear in sand layer, differential flow in viscous layer; (d-f) Longitudinal strain in the x-direction (e_{xx}): warm colours represent extension, cold colours represent contraction; (g-i) Shear strain (e_{xy}) in the xy-section plane: Warm colours represent sinistral shear, cold colours represent dextral shear; (j-l) Longitudinal strain in z-direction (e_{zz}): Warm colours represent extension, cold colours represent contraction. The locations of sections I, II and III are close to those of sections 3, 4 and 6 in Figs. 5d and 6a.

Figure 11.

DVC total displacement analysis of Model C (orthogonal extension, sedimentation) (a-c) 3D displacement; (d-f) Horizontal displacement in the xy-plane, parallel to the extension direction. Warm colours represent displacement to the left, cold colours represent displacement to the right; (g-i) Vertical velocities. Warm colours represent uplift, cold colours represent subsidence; (j-l) Horizontal displacement in the z-direction (normal to section and extension direction). Warm colours represent displacement towards the observer, cold colours represent displacement away from the observer. The locations of sections I, II and III are close to those of sections 9, 11 and 13 in Figs. 5h and 6b.

Figure 12.

Overview of Model I (without sedimentation) and Model J (with sedimentation) from series 2. Set-up: 15˚ oblique extension, secondary seed and rift underlap (φ = 75˚). (a-d and e-h) Top view results with time. (a'-d' and e'-h') Horizontal CT sections, at 2 cm depth (see i). (i-j) CT sections, illustrating the final internal model structure. Section locations are shown in d-d' and h-h' for Models I and J respectively.

Figure 13.

Overview of Model M (without sedimentation) and Model N (with sedimentation) from series 3. Set-up: -30˚ (sinistral) oblique extension, secondary seed and rift underlap (φ = 25˚). (a-d and e-h) Top view results with time. (a'-d' and e'-h') Horizontal CT sections, at 2 cm depth (see i). (i-j) CT sections, illustrating the final internal model structure. Section locations are shown in d-d' and h-h' for Models M and N respectively.

ACCEPTED MANUSCRIPT

Figure 14.

Schematic overview summarizing the influence sedimentation could have on rift evolution, based on our models. A strength profile is shown to the right of each image. (a) Rift initiation: extension and normal faulting in the undeformed upper crust. (b-c) Rift evolution without sediment influx: deep topography, high fault density due to weakening of the upper crust, rising lower crust (and mantle?) and early rupture of the upper crust. (b'-c') Rift evolution with sediment influx: strong subsidence, but rift basin fills up to form flat topography, low fault density due to upper crust strengthening, limited rising of the lower crust (and mantle?) and postponed rupture of the upper crust.

Figure 15.

Schematic depiction of the brittle and viscous deformation in a rift pass setting as observed in our models (compare with Fig. 4a). (a) Map view of brittle displacement, involving an extension gradient occurring along both propagating rift basins causing a rotation of the rift pass block as indicated by the deformed lines that were initially parallel. (b) Material flow in the viscous layer beneath the brittle cover. Material moves towards the developing rifts. Motion is dominantly perpendicular to the rift, but it contains also a rift-parallel component, from the rift tip to the more developed sections of the rift.

Figure. 16

(a) North Sea Jurassic rifts. (b) En-echelon left-stepping basins and intra-basin horsts and rift passes in the Central Graben. Approximate extension direction is shown by red arrows. White dotted lines illustrate rift basin orientation. Modified after Erratt et al. (1999)

Figure 17.

Evolution of the Mandal High in the North Sea in (a) the Permian, (b). Triassic, (c) Late Jurassic, (d) Cretaceous and (e) Cenozoic. Modified after Rossland et al., 2013. AAPG©2013, reprinted by permission of the AAPG, whose permission is required for further use.

ACCEPTED MANUSCRIPT

Appendix A

Figure A1.

Strain charts of xy-sections derived from finite 3D strain of Model C (orthogonal extension, sedimentation) obtained through DVC analysis. (a-c) 3D shear strain (positive values only): Higher values show more deformed areas (localised shear in sand layer, differential flow in viscous layer; (d-f) Longitudinal strain in the x-direction (e_{xx}): Warm colours represent extension, cold colours represent contraction; (g-i) Shear strain (e_{xy}) in the xy-section plane: Warm colours represent sinistral shear, cold colours represent dextral shear; (j-l) Longitudinal strain in z-direction (e_{zz}): Warm colours represent extension, cold colours represent contraction. The locations of sections I, II and III are close to those of sections 9, 11 and 13 in Figs. 4.5h and 4.6b.

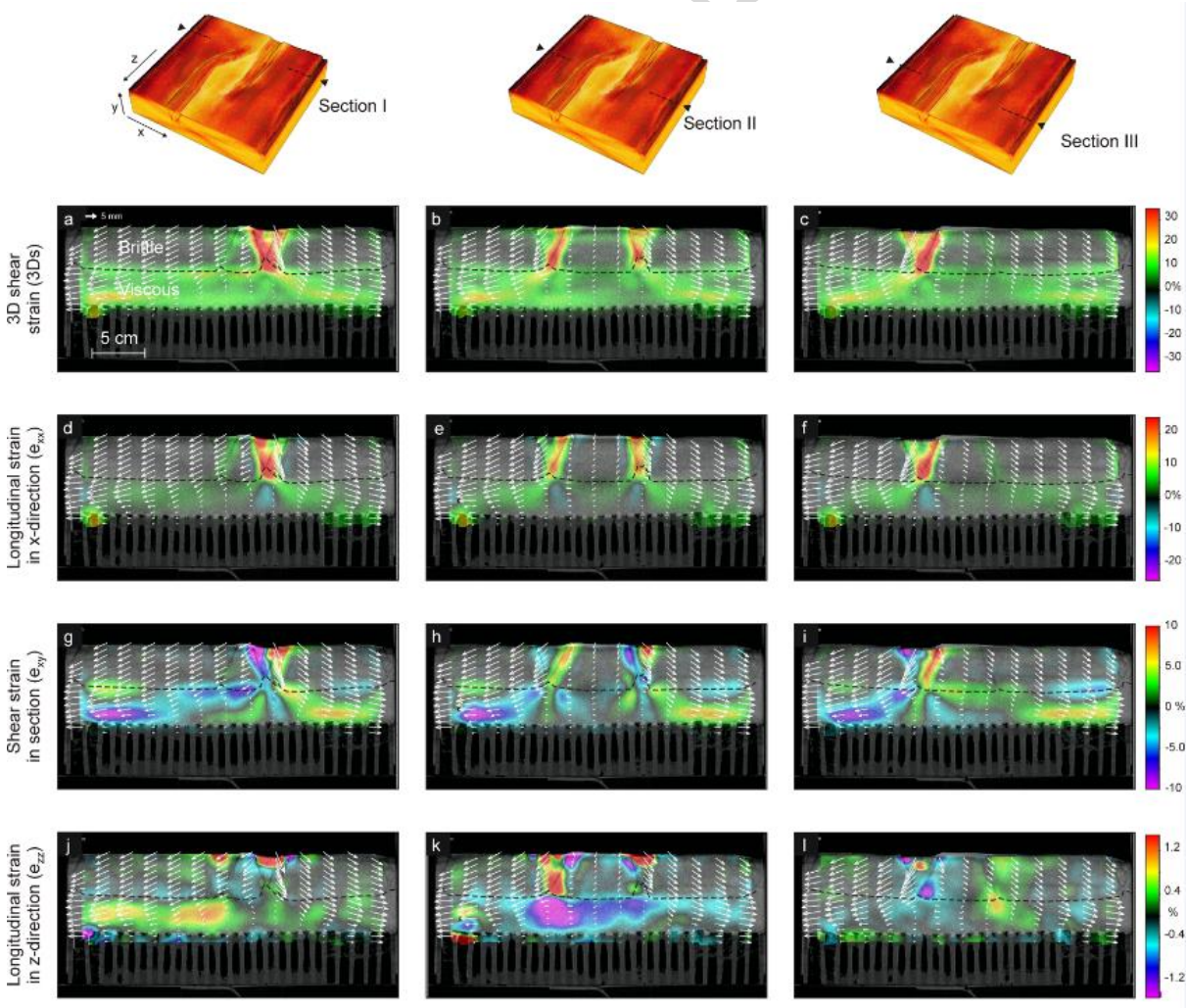

ACCEPTED MANUSCRIPT

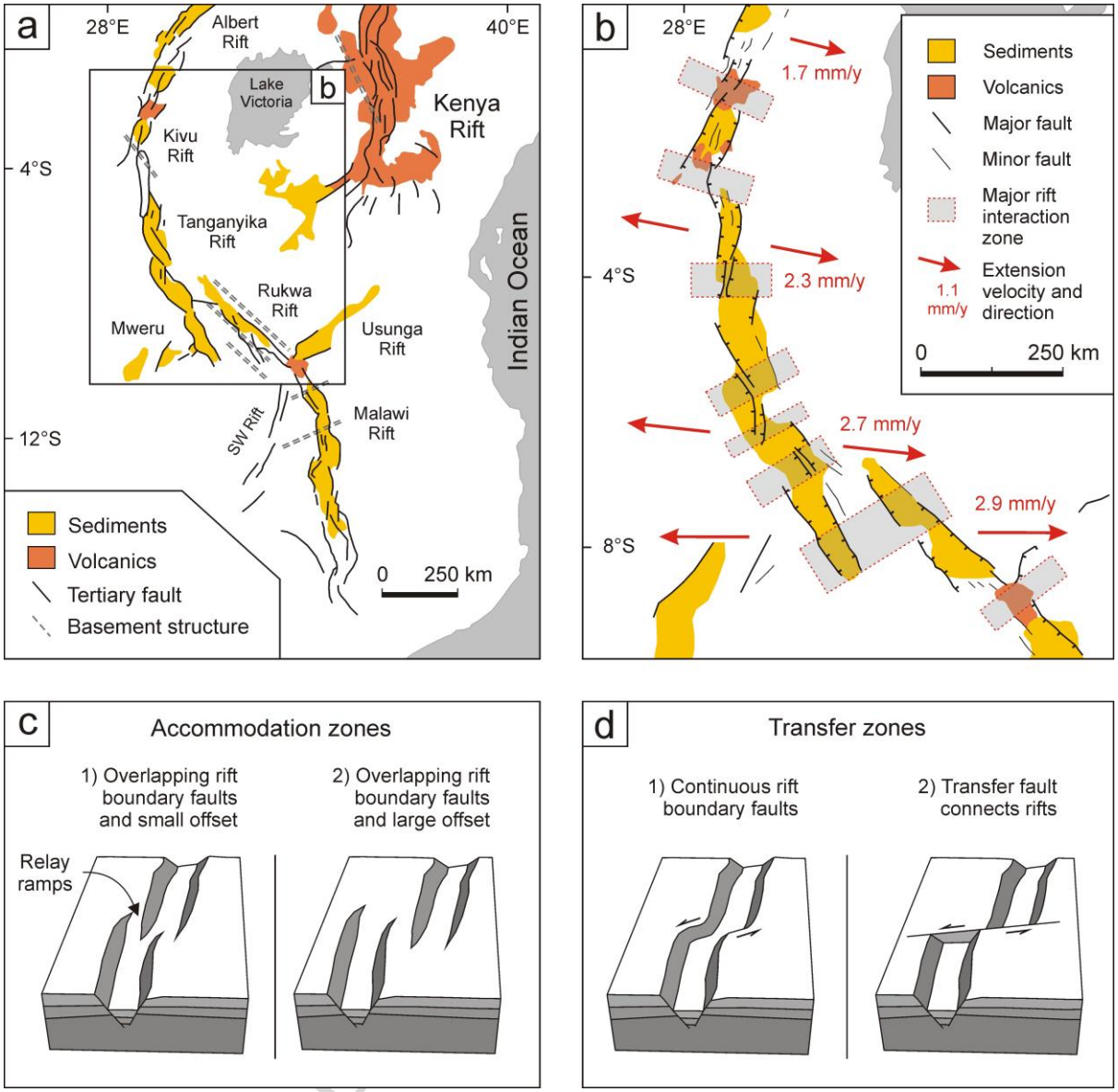

Figure 1

ACCEPTED

ACCEPTED MANUSCRIPT

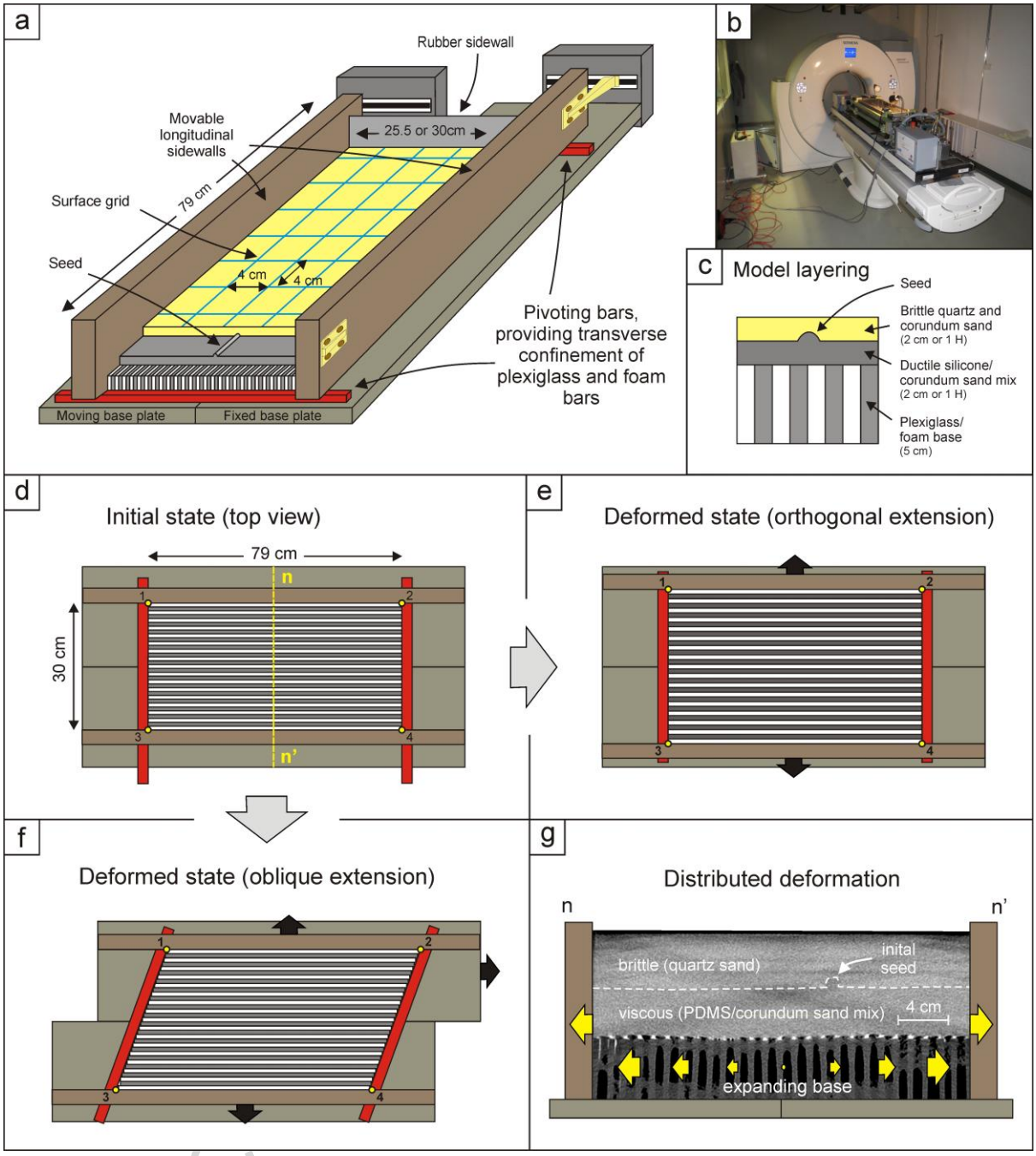

ACCEPTED MANUSCRIPT

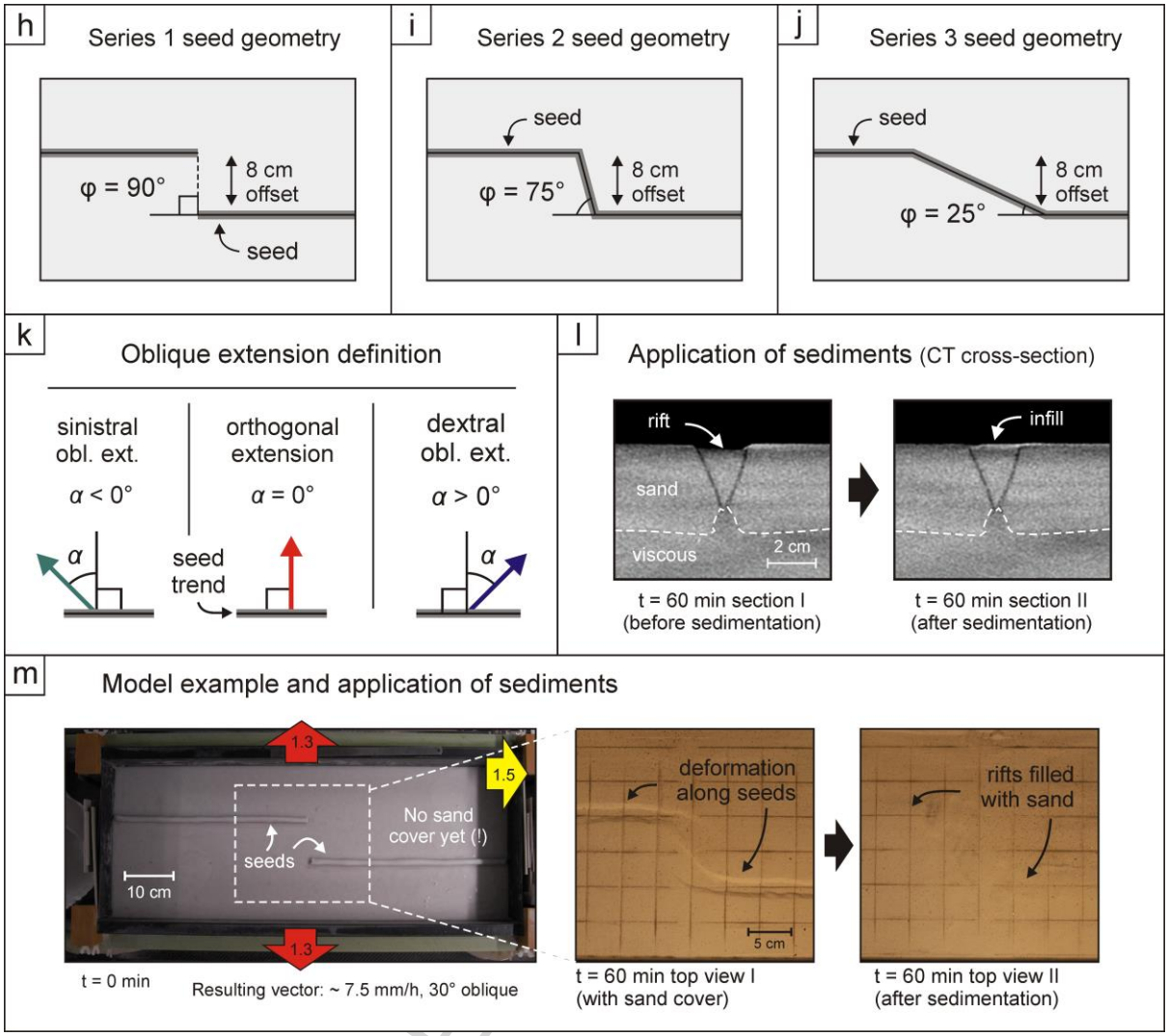

Figure 2

ACCEPTED

ACCEPTED MANUSCRIPT

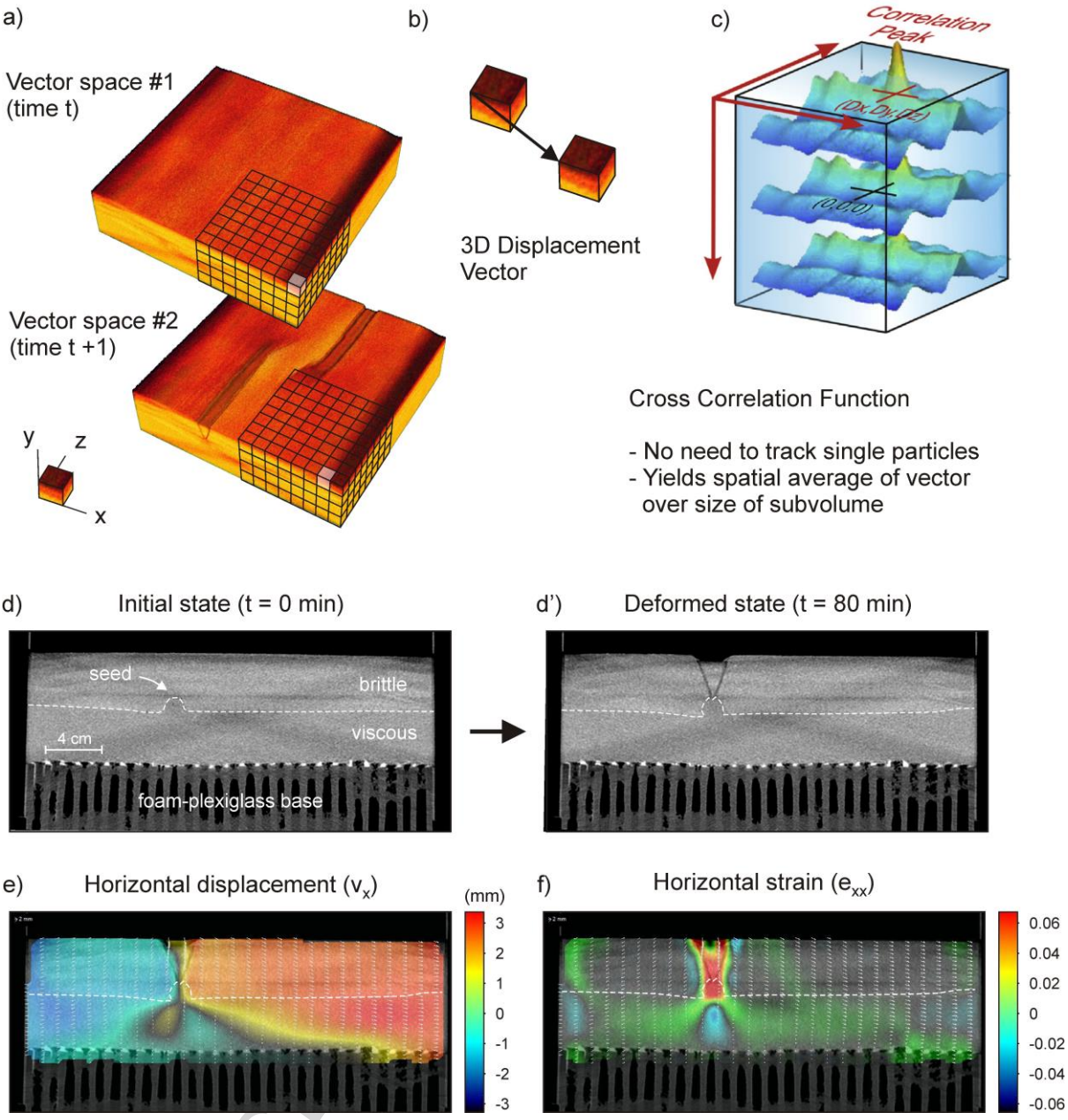

Figure 3

ACCEPTED MANUSCRIPT

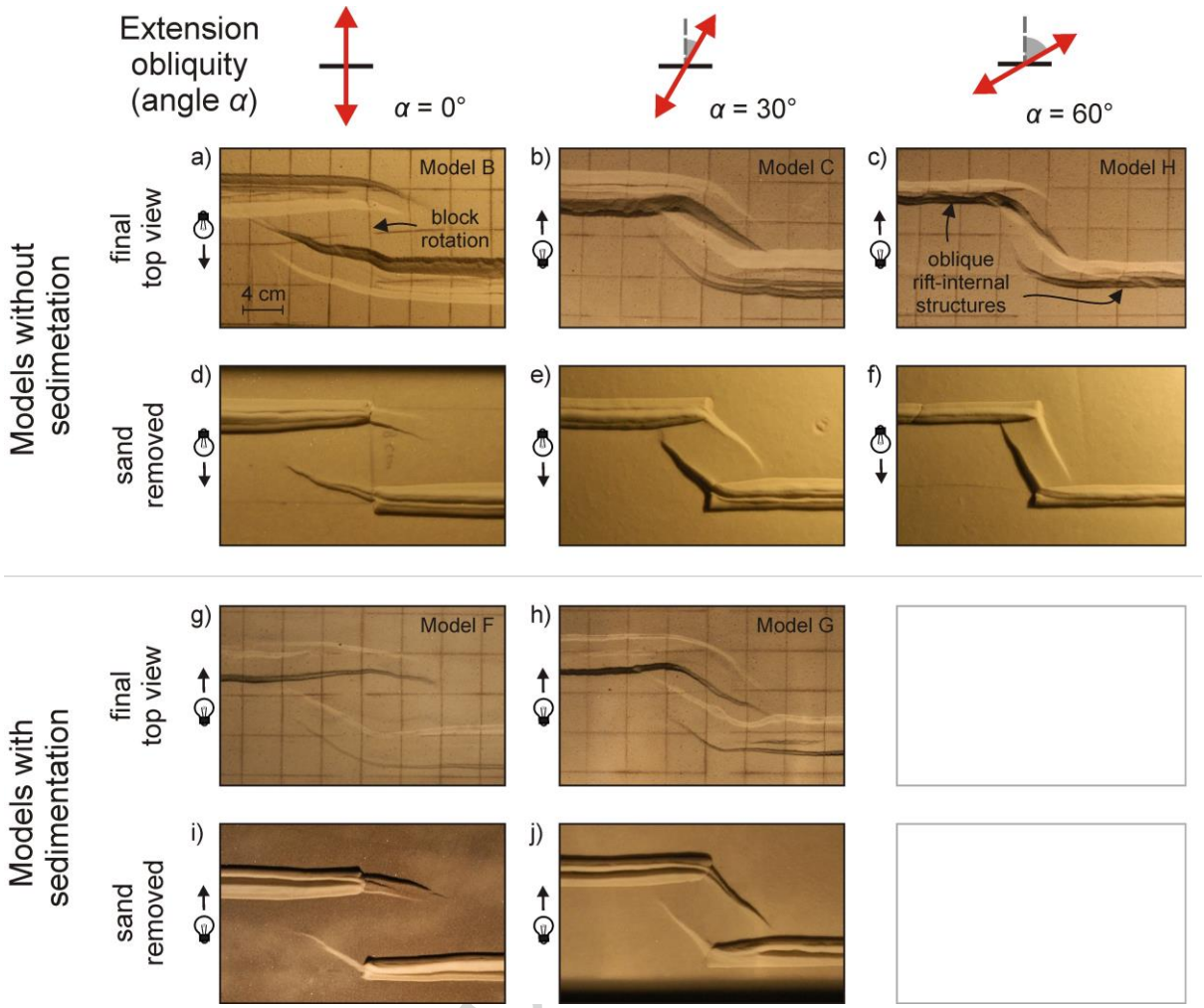

Figure 4

ACCEPTED

ACCEPTED MANUSCRIPT

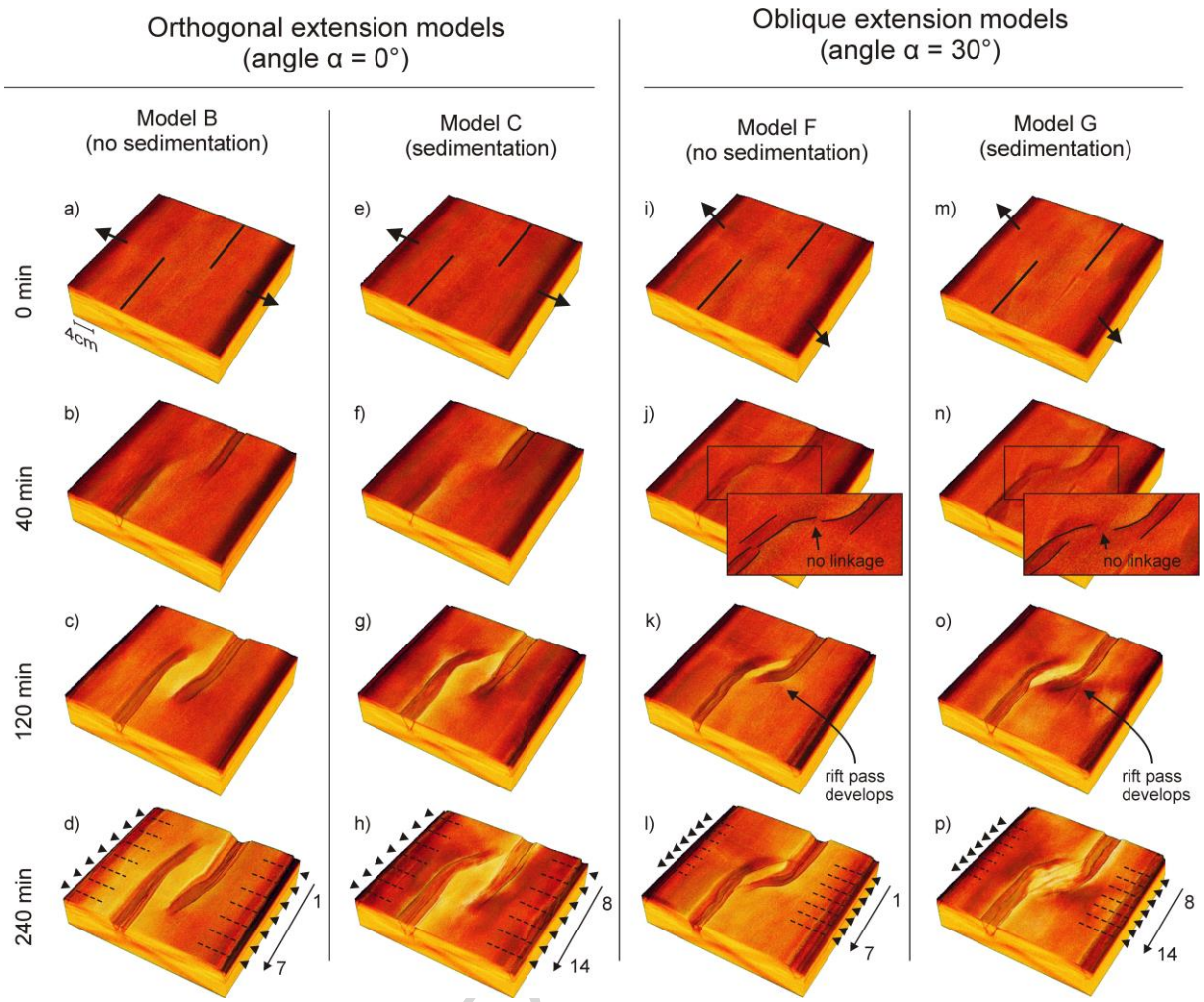

Figure 5

ACCEPTED

ACCEPTED MANUSCRIPT

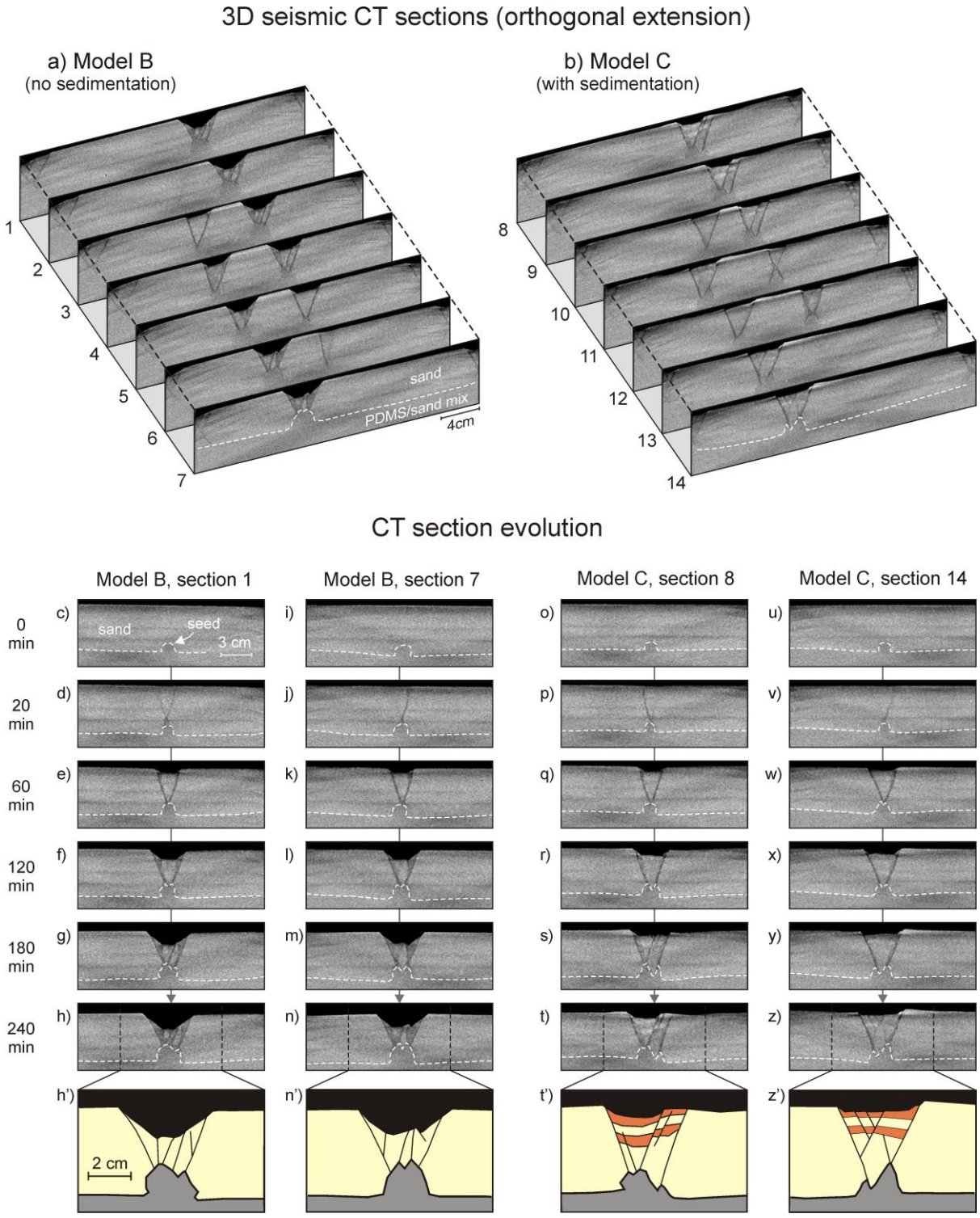

Figure 6

ACCEPTED MANUSCRIPT

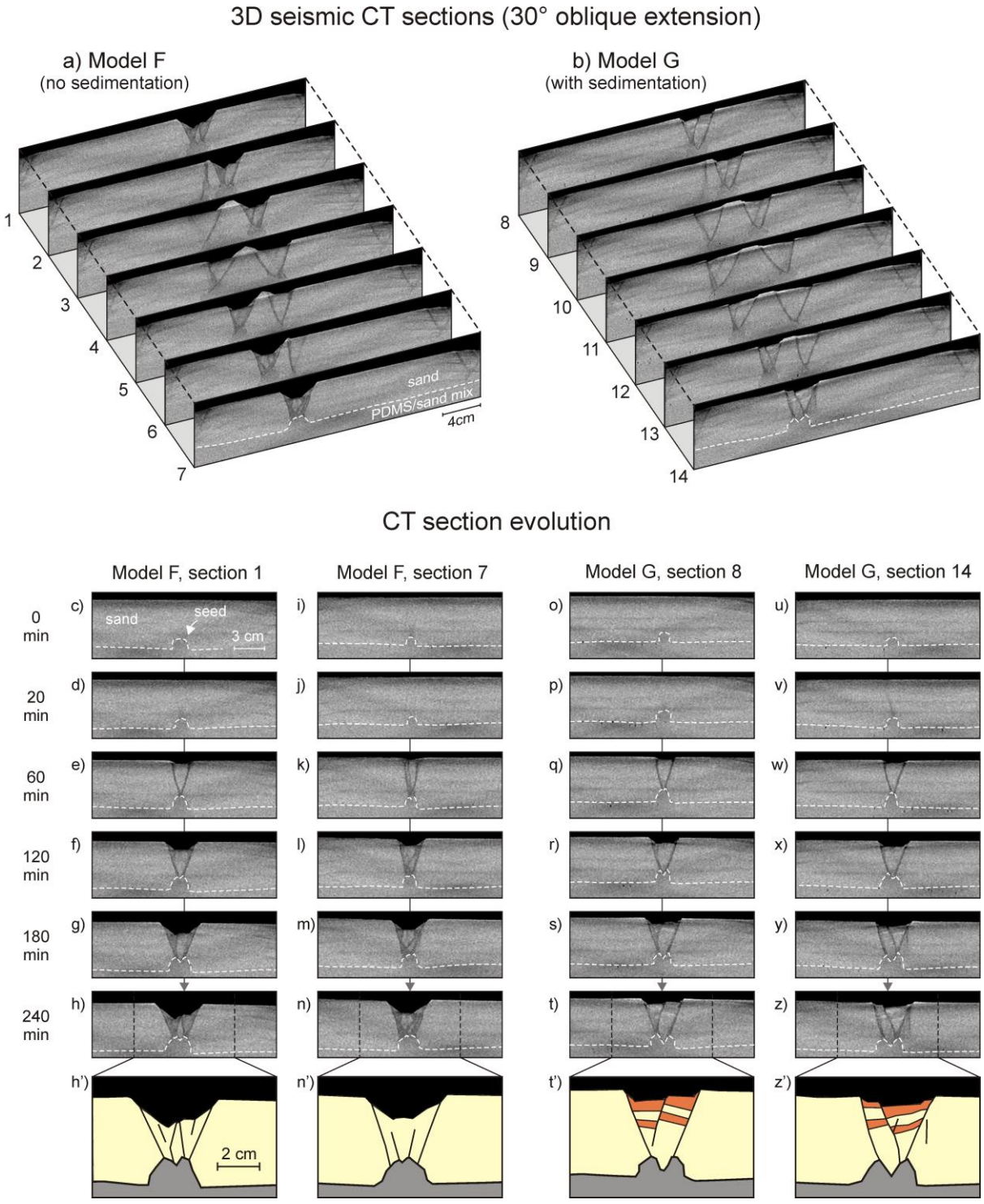

Figure 7

ACCEPTED MANUSCRIPT

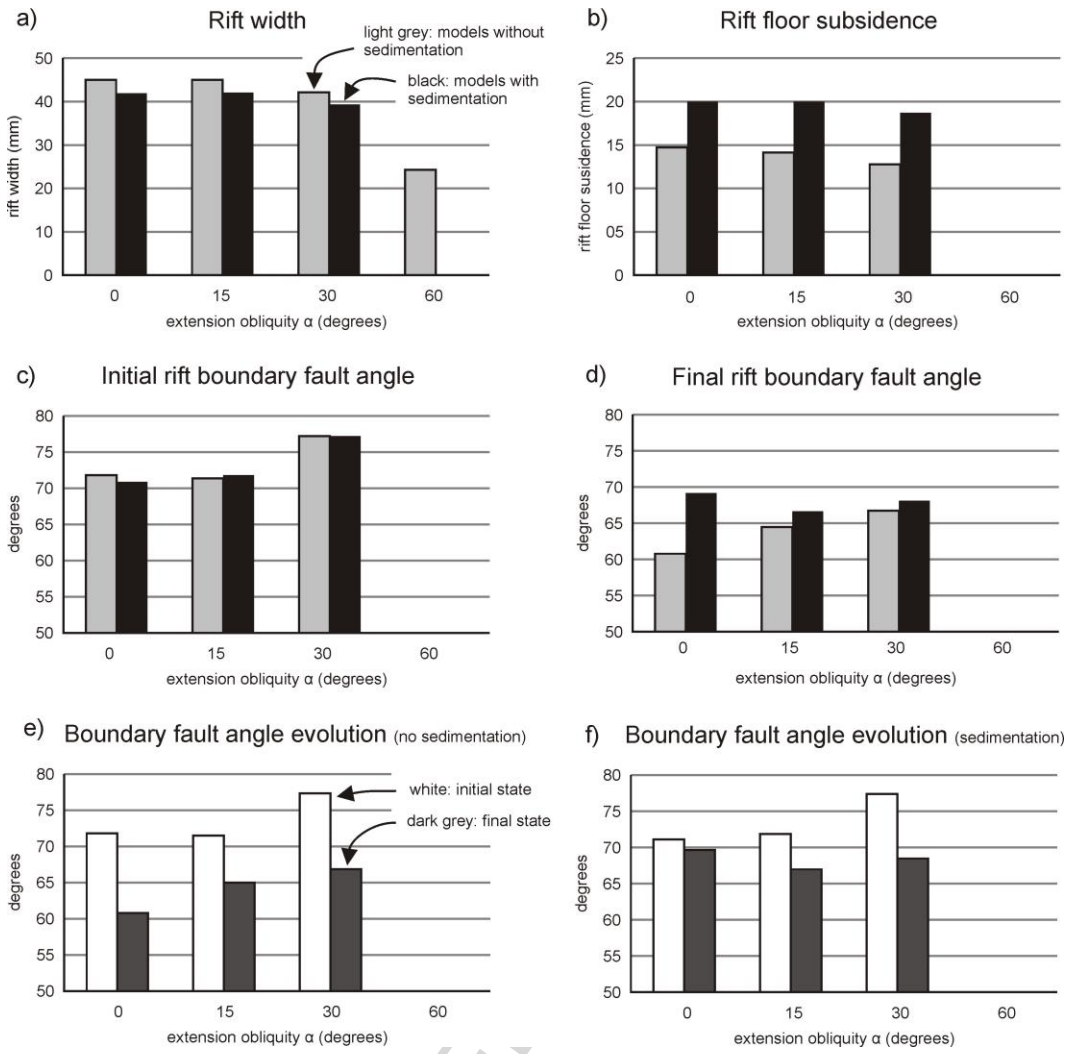

Figure 8

ACCEPTED

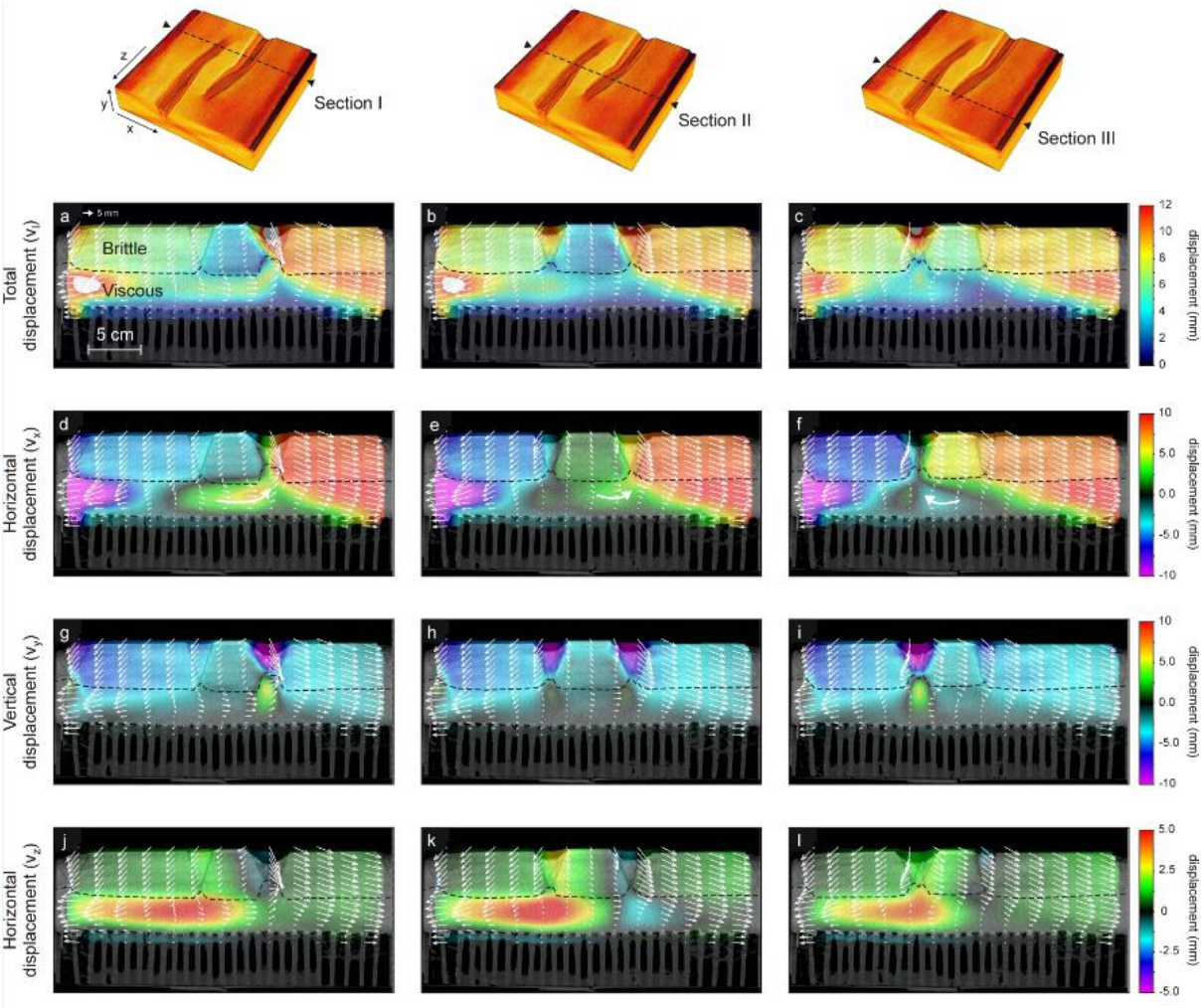

Figure 9

ACCEPTED

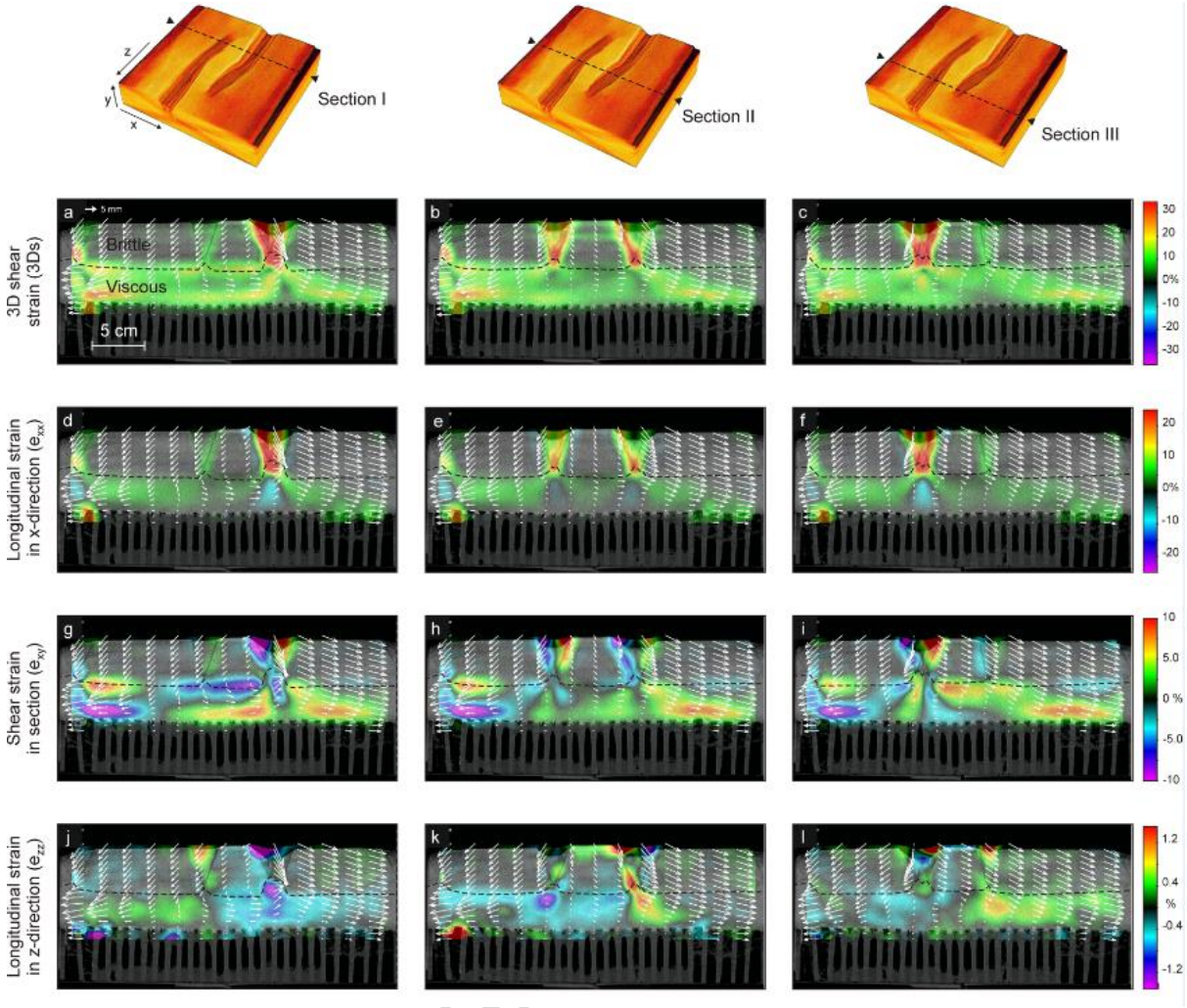

Figure 10

ACCEPTED

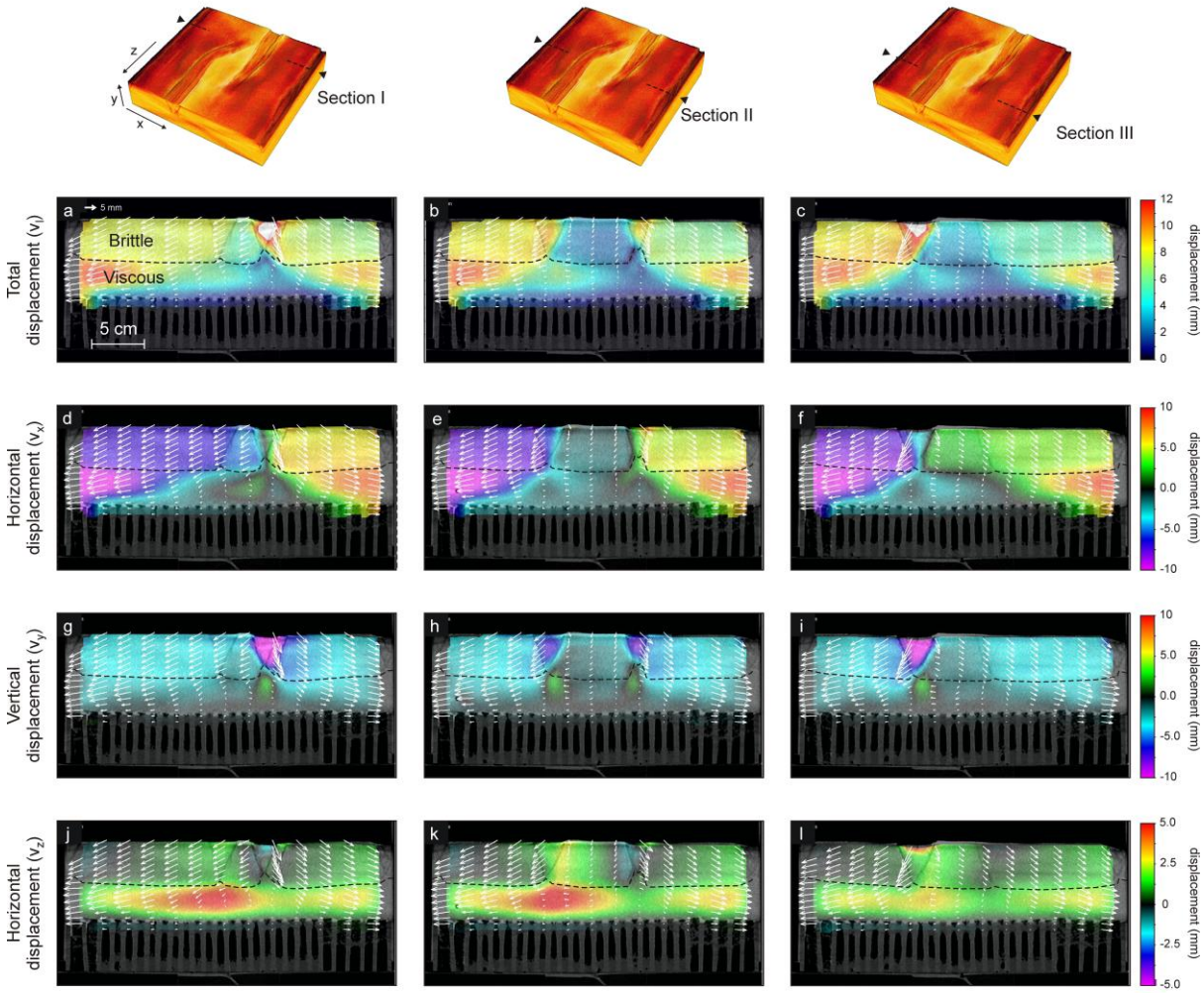

Figure 11

ACCEPTED

ACCEPTED MANUSCRIPT

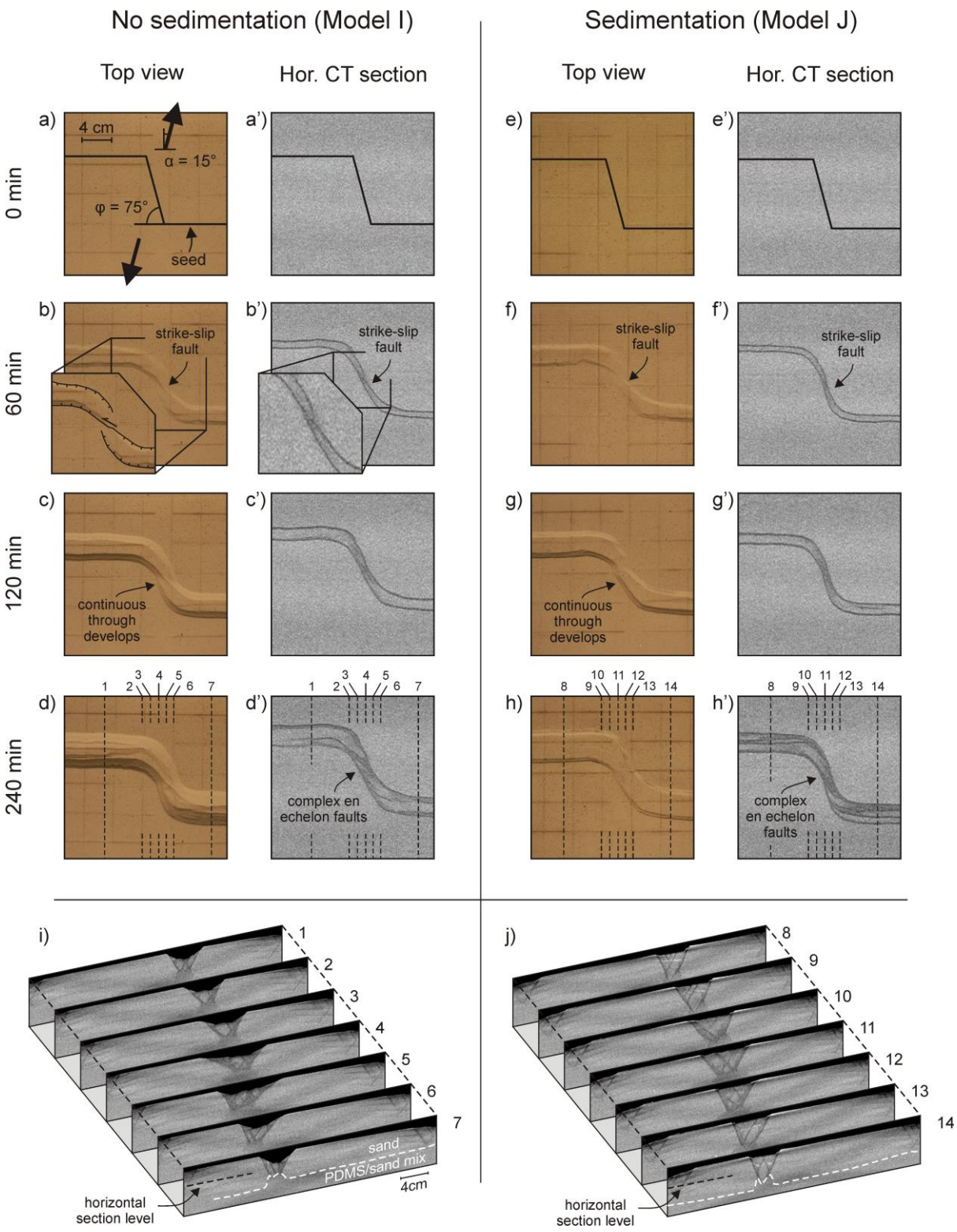

Figure 12

ACCEPTED MANUSCRIPT

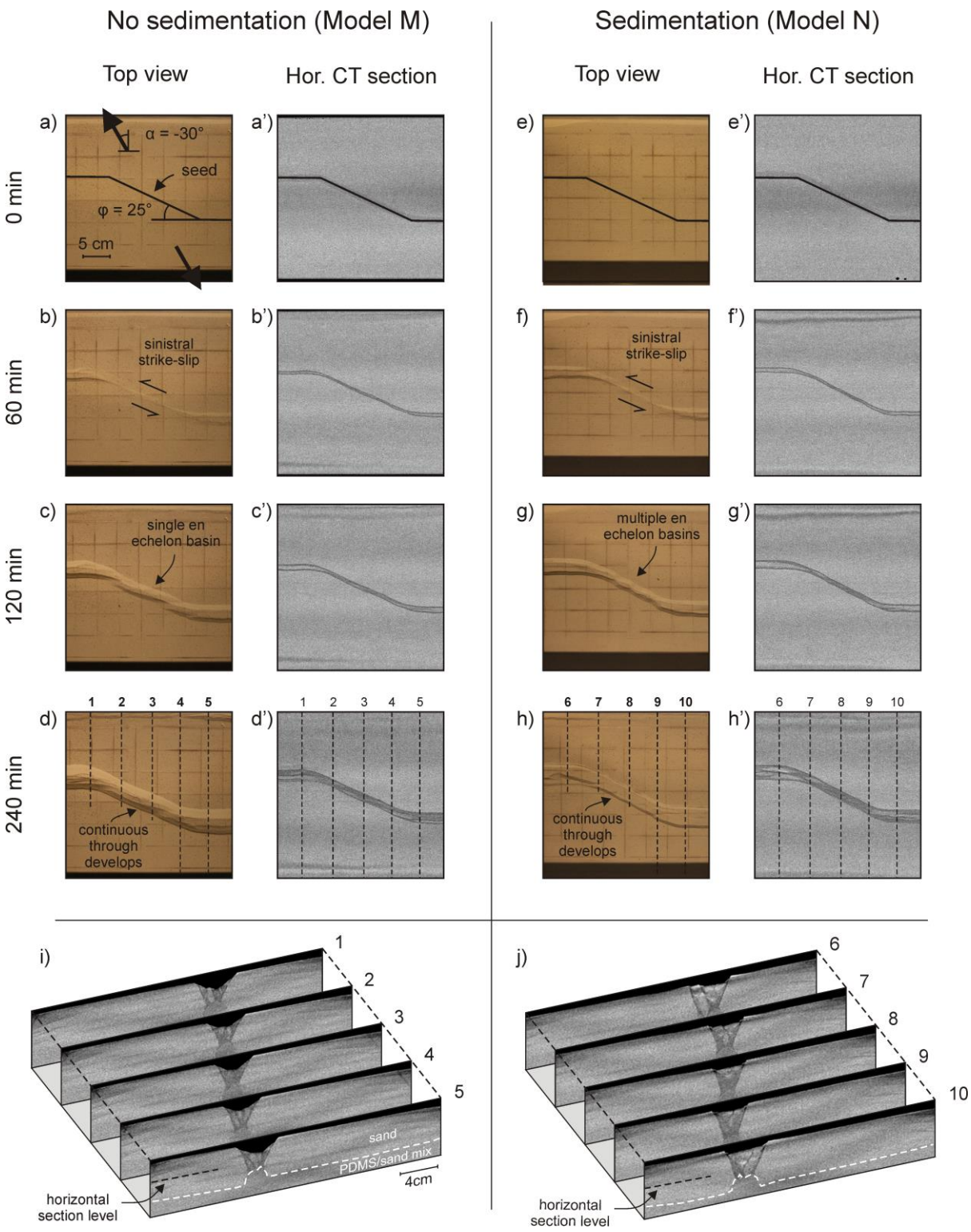

Figure 13

ACCEPTED MANUSCRIPT

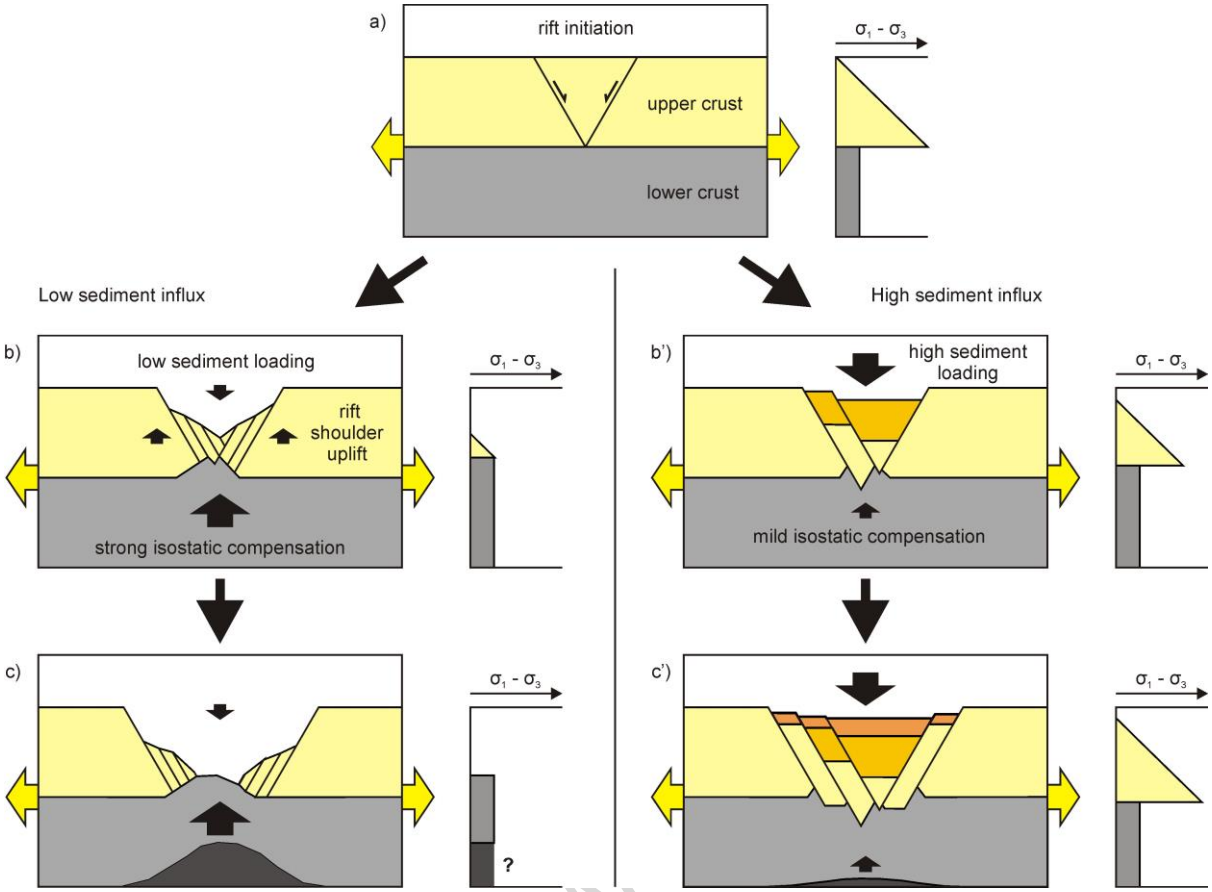

Figure 14

ACCEPTED MANUSCRIPT

ACCEPTED MANUSCRIPT

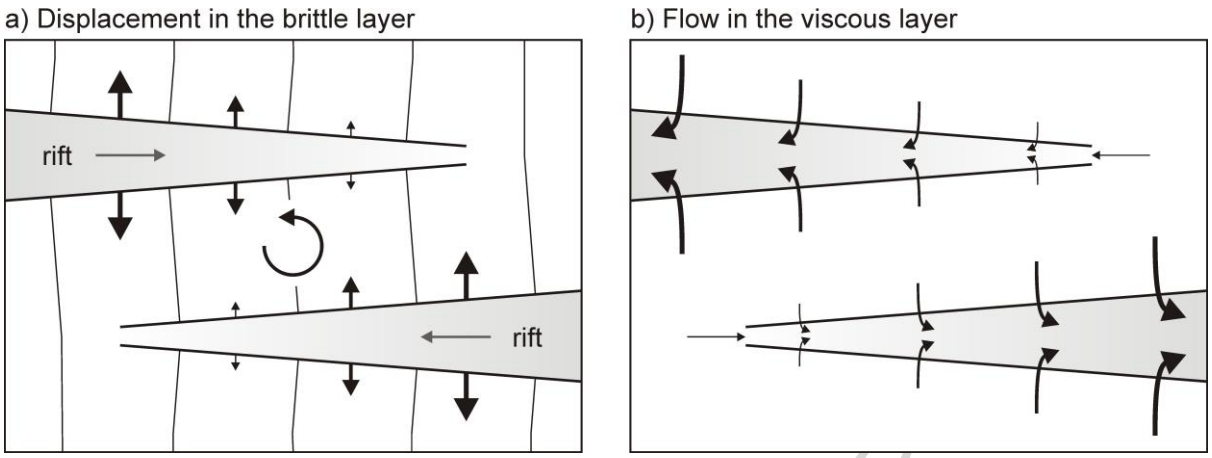

Figure 15

ACCEPTED MANUSCRIPT

ACCEPTED MANUSCRIPT

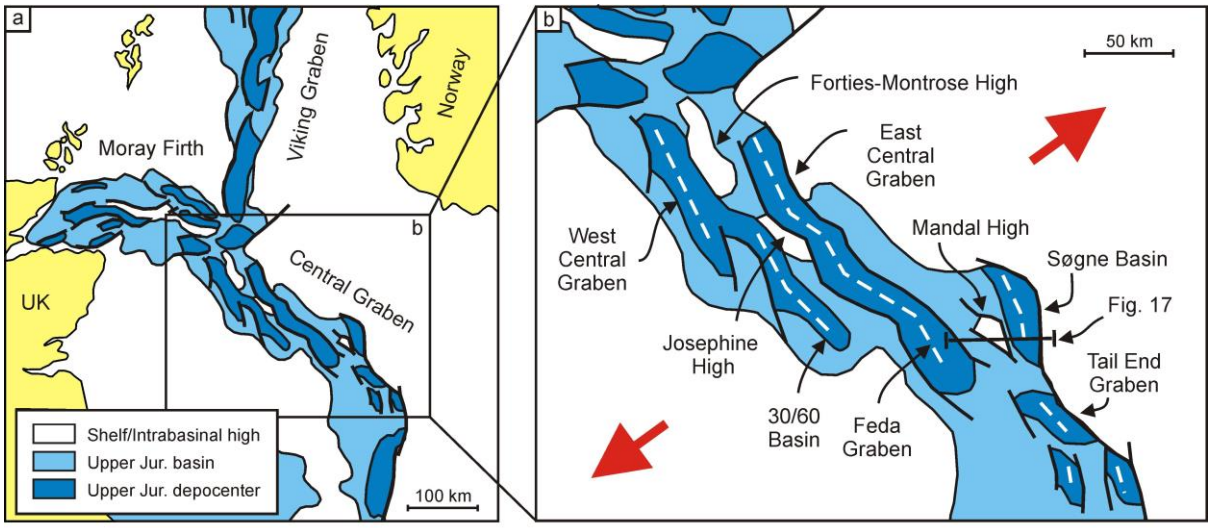

Figure 16

ACCEPTED MANUSCRIPT

ACCEPTED MANUSCRIPT

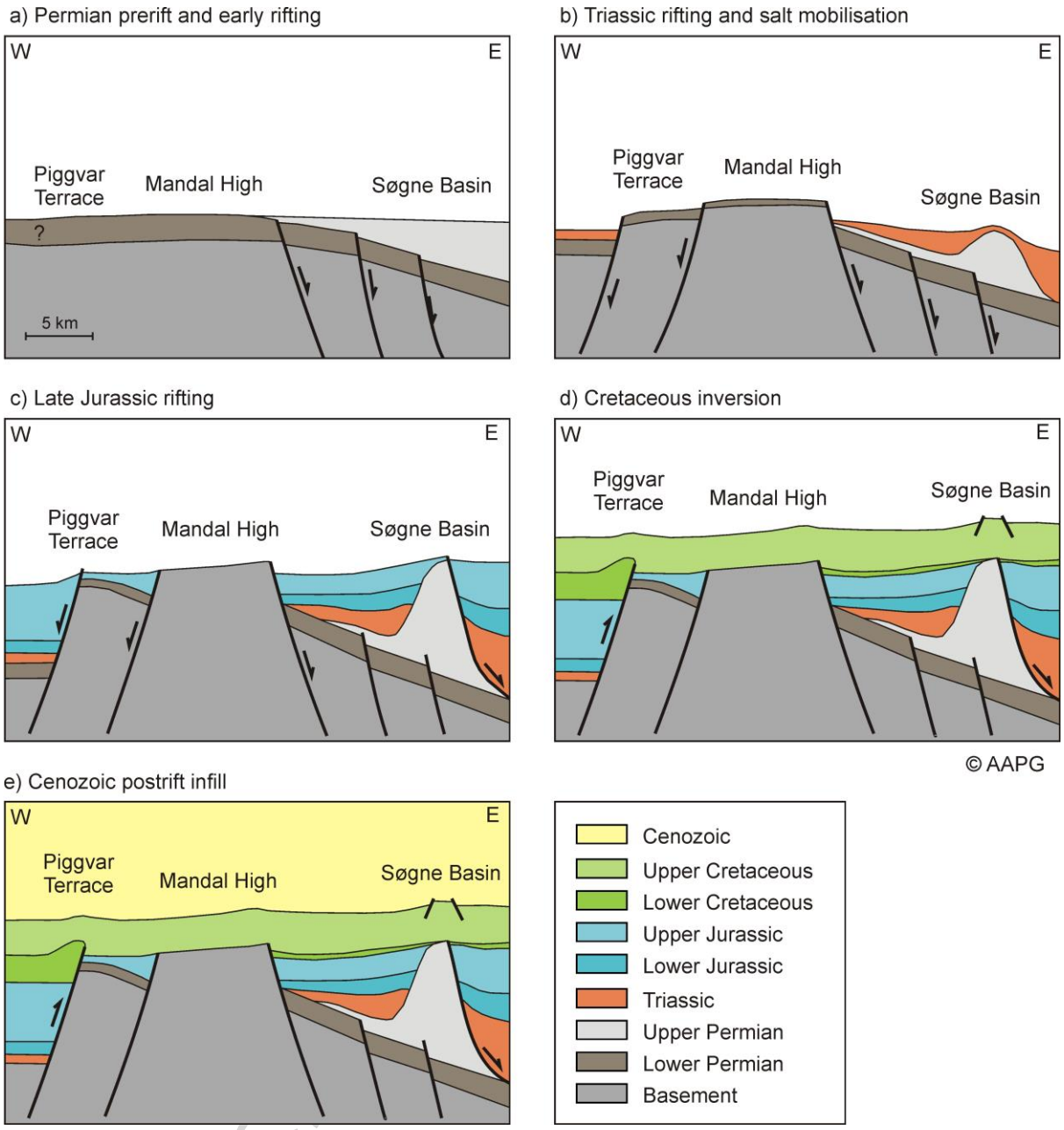

Figure 17

ACCEPTED MANUSCRIPT

Table 1

Granular materials	**Quartz sand[a]**	**Corundum sand[b]**	**Zirshot[c]**
Grain size range	60-250 μm	88-175 μm	150-210 μm
Bulk density (sieved)	1560 kg/m^3	1890 kg/m^3	ca. 2300 kg/m^3
Angle of internal peak friction	36.1˚	37˚	-
Angle of dynamic-stable friction	31.4˚	32˚	-
Cohesion	9 ± 98 Pa	39 ± 10 Pa	-
Viscous material	**PDMS/corundum sand mixture[a]**		
Weight ratio PDMS : corundum sand	0.965 kg : 1.00 kg		
Mixture density	ca. 1600 kg/m^3		
Viscosity[d]	ca. $1.5 \cdot 10^5$ Pa·s		
Type	near-Newtonian (n = 1.05)[e]		

a Quartz sand and viscous mixture characteristics after Zwaan and Schreurs (2016)
b Corundum sand characteristics after Panien et al. (2006) and Klinkmüller (2011)
c Zirshot properties after Carlo AG (2017)
d The viscosity value holds for model strain rates < 10^{-4} s^{-1}
e Stress exponent n (dimensionless) represents sensitivity to strain rate

ACCEPTED MANUSCRIPT

ACCEPTED MANUSCRIPT

Table 2

	Model	Extension obliquity (alpha)	Seed geometry (phi)	Secondary seed	Sedimentation	CT-scanned	Shown in
Series 1	A	0°	90°	-	-	-	-
	B	0°	90°	-	-	X	Figs. 3-6, 9-10
	C	0°	90°	-	X	X	Figs. 4-6, 11, A1
	D	30°	90°	-	-	-	-
	E	30°	90°	-	X	-	-
	F	30°	90°	-	-	X	Figs. 4, 5, 7
	G	30°	90°	-	X	X	Figs. 2, 4, 5, 7
	H	60°	90°	-	-	-	Fig. 4
S2	I	15°	75°	X	-	X	Fig. 12
	J	15°	75°	X	X	X	Fig. 12
Series 3	K	-30°	25°	-	-	-	-
	L	-30°	25°	X	X	-	-
	M	-30°	25°	X	-	X	Fig. 13
	N	-30°	25°	X	X	X	Fig. 13

ACCEPTED MANUSCRIPT

ACCEPTED MANUSCRIPT

Table 3

	General parameters			**Brittle upper crust**		**Ductile lower crust**		**Dynamic scaling values**	
	Gravitational acceleration g (m/s^2)	Crustal thickness h (m)	Extension velocity v (m/s)	Density ρ (kg/m^3)	Cohesion C (Pa)	Density ρ (kg/m^3)	Viscosity η (Pa·s)	Rambergnumber R_m	Brittle stress ratio R_s
Model	9.81	0.08	$2.1 \cdot 10^{-6}$	1560	9	1600	$1.5 \cdot 10^{5}$	80	25.5
Nature	9.81	$4 \cdot 10^{4}$	$1 \cdot 10^{-10}$	2800	$7 \cdot 10^{7}$ [a]	2900	$1 \cdot 10^{21}$	120	9.2

a Cohesion value after Corti et al. (2004)

ACCEPTED MANUSCRIPT

ACCEPTED MANUSCRIPT

Highlights:

- Syn-rift sedimentation does not significantly influence large-scale rift structures
- Yet sedimentary loading effects can strongly influence internal rift structures
- Extension direction and inherited structures largely control how rifts connect
- DVC can now quantify full 3D deformation in brittle-viscous analogue models
- Material may also move out of plane under orthogonal extension conditions

ACCEPTED MANUSCRIPT